

# Geochemical characteristics and Sr–Nd–Hf isotope compositions of mantle xenoliths and host basalts from Assab, Eritrea: implications for the composition and thermal structure of the lithosphere beneath the Afar Depression

Mengist Teklay · Erik E. Scherer · Klaus Mezger · Leonid Danyushevsky

Received: 25 February 2009 / Accepted: 1 October 2009 / Published online: 24 October 2009  
© The Author(s) 2009. This article is published with open access at Springerlink.com

**Abstract** The Afar Depression offers a rare opportunity to study the geodynamic evolution of a rift system from continental rifting to sea floor spreading. This study presents geochemical data for crustal and mantle xenoliths and their alkaline host basalts from the region. The basalts have enriched REE patterns, OIB-like trace element characteristics, and a limited range in isotopic composition ( $^{87}\text{Sr}/^{86}\text{Sr} = 0.70336\text{--}0.70356$ ,  $\varepsilon_{\text{Nd}} = +6.6$  to  $+7.0$ , and  $\varepsilon_{\text{Hf}} = +10.0$  to  $+10.7$ ). In terms of trace elements and Sr–Nd isotopes, they are similar to basalts from the Hanish and Zubair islands in the southern Red Sea and are thus interpreted to be melts from the Afar mantle. The gabbroic crustal xenoliths vary widely in isotope composition ( $^{87}\text{Sr}/^{86}\text{Sr} = 0.70437\text{--}0.70791$ ,  $\varepsilon_{\text{Nd}} = -8.1$  to  $+2.5$ , and  $\varepsilon_{\text{Hf}} = -10.5$  to  $+4.9$ ), and their trace element characteristics match those of Neoproterozoic rocks from the Arabian–Nubian Shield and modern arc rocks, suggesting that the lower crust beneath the Afar Depression contains Neoproterozoic mafic igneous rocks. Ultramafic mantle xenoliths from Assab contain primary assemblages of fresh

ol + opx + cpx + sp  $\pm$  pl, with no alteration or hydrous minerals. They equilibrated at 870–1,040°C and follow a steep geothermal gradient consistent with the tectonic environment of the Afar Depression. The systematic variations in major and trace elements among the Assab mantle xenoliths together with their isotopic compositions suggest that these rocks are not mantle residues but rather series of layered cumulate sills that crystallized from a relatively enriched picritic melt related to the Afar plume that was emplaced before the eruption of the host basalts.

**Keywords** Afar Depression · Xenoliths · Cumulates · Rifting · Sr–Nd–Hf isotopes

## Introduction

Mantle xenoliths, together with orogenic peridotites, represent the only direct samples of the mantle. Due to their rapid eruption, these rocks usually freeze in the mineralogical and chemical signatures that they acquired during crystallization or re-equilibration at their depth of origin. Hence, they provide crucial evidence of the nature of the lithospheric mantle at the time of their eruption (e.g., Pearson et al. 2004 and references therein). Mantle xenoliths from continental rift areas, in addition to sampling very thin lithosphere, can constrain the local geothermal gradient and the extent of interaction between asthenosphere and lithosphere. Furthermore, they can supply direct compositional information on deep-seated sources and may constrain the metasomatic history and  $P$ – $T$  conditions of melting, which are important parameters associated with the rifting process. A promising area for the study of continental rifting processes and the transition between continental rifting and sea floor spreading is the Afar

Communicated by J. Hoefs.

**Electronic supplementary material** The online version of this article (doi:10.1007/s00410-009-0451-0) contains supplementary material, which is available to authorized users.

M. Teklay  
Department of Earth Sciences, University of Asmara,  
Asmara, Eritrea

M. Teklay · E. E. Scherer · K. Mezger (✉)  
Institut für Mineralogie, Universität Münster, Münster, Germany  
e-mail: klaush@nwz.uni-muenster.de;  
klaus.mezger@geo.unibe.ch

L. Danyushevsky  
CODES, University of Tasmania, Tasmania, Australia

volcanic province, because it is actively undergoing continental break-up.

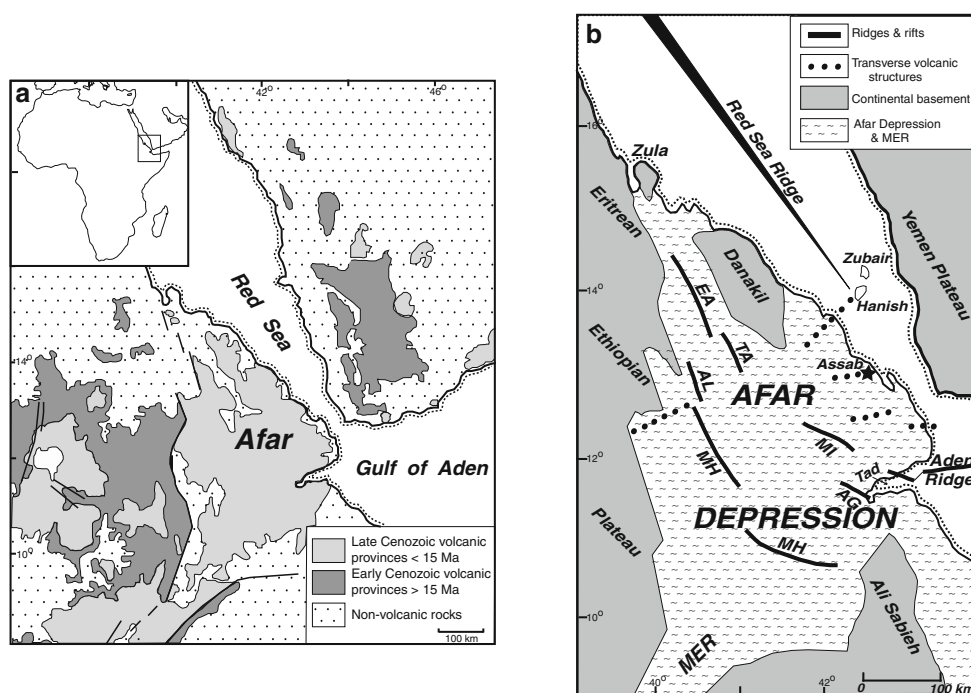
The Afar volcanic province is the second youngest large igneous province worldwide and its magmatic activity coincided with the onset of rifting of Arabia from Africa, a process that continues along the Red Sea and Gulf of Aden axes, and in the Afar Depression. The Afar Depression, whose tectonic and magmatic activity is attributed to a deep-seated mantle plume that impinged upon the lithosphere at 30 Ma, represents the advanced transitional stage between continental rifting and sea floor spreading, and constitutes one of the largest currently active continental igneous provinces (e.g., Schilling et al. 1992; Hoffman et al. 1997). Hence, the Afar Depression offers the unique opportunity for studying the geodynamic evolution of a major rift system from continental break-up to sea floor spreading.

New geochemical and Sr–Nd–Hf isotope data for host basalts, crustal xenoliths, and mineral separates from mantle xenoliths from the Assab area of the Afar Depression document and constrain the chemical and isotopic signature of the lithosphere beneath Afar and the potential relationship between the Assab rocks and mantle xenoliths from Ethiopia, Yemen, Saudi Arabia, Egypt, and Jordan. The data are also used to evaluate the potential contributions of the lithospheric mantle as a source of flood and intraplate volcanism and to unravel the petrogenesis of the Assab mantle xenoliths, addressing the question of whether they represent cumulates or residues.

## Geologic setting

The Afar Depression is the triple-rift junction of the Red Sea, Gulf of Aden and East African rift systems (Fig. 1) and has been subjected to rapid crustal spreading as evidenced by numerous NNW–SSE fissures (Fig. 1). With the exception of the Danakil block in Eritrea and the Ali Sabieh block in Djibouti, it is floored by dominantly basaltic volcanic rocks that are related to rifting (Pilger and Rösler 1975). Basement rocks, Neoproterozoic metamorphic rocks of the Arabian–Nubian Shield, and Paleozoic–Mesozoic sedimentary strata crop out only in the Danakil and Ali Sabieh blocks. With the exception of these older rocks, the surface of the Afar region consists only of volcanic rocks, Upper Tertiary continental and lacustrine sediments, and Quaternary marine sediments (Barberi and Varet 1977). The oldest volcanic rocks (>4 Ma) crop out mainly in the Ali Sabieh block and south of the Danakil block (Barberi and Varet 1977; Audin et al. 2004). These are overlain by the Afar stratoid series (<4 Ma; Civetta et al. 1974; Audin et al. 2004 and references therein), which is exposed throughout the depression. Younger fissural basalts overlie the Afar stratoid series along the axial ranges (<1 Ma; Manighetti et al. 2001) and at the edges of the depression along the transverse tectonic trends (Fig. 1). The tectonic structures and volcanic activity in the axial range are manifestations of a propagating rift that extends from the Red Sea to the East African rift (Barberi and Varet 1977).

**Fig. 1** **a** Distribution of Cenozoic volcanism in part of the Afar volcanic province (modified after Pik et al. 1998; Bertrand et al. 2003; Ukstins Peate et al. 2005) and **b** schematic structural map of Afar Depression (modified after Barberi and Varet 1977; Manighetti et al. 1998) showing study area (*star*). EA Erta’Ale, TA Tat’Ali, AL Alayta, MH Manda Hararo, MI Manda Inakir, AG Asal-Ghoubbet, Tad Gulf of Tadjoura, MER Main Ethiopian Rift



Transverse activity (<1 Ma) was most intense south of the Danakil block (Civetta et al. 1975) including the Assab range volcanic area, located between the central Afar Depression and the Red Sea (Fig. 1). These are recent volcanic rocks located along E–W fracture systems that are transversal relative to the main NNW trend of the depression. Civetta et al. (1974) have reported a 0.6 Ma K–Ar age and a 0.285 Ma  $^{230}\text{Th}$  age for the Assab transverse volcanic range rocks. The composition of these lavas ranges from ankaramitic to hawaiitic basalt (De Fino et al. 1973). Thus, in contrast to the axial range of central Afar, which is characterized by intense NNW–SSE tectonic activity and a less alkaline (transitional) volcanism, the less faulted Assab area is characterized by transverse E–W tectonics and by markedly more alkaline volcanism. Civetta et al. (1974, 1975) have suggested that the marginal alkalic basalts erupted through a thin continental-type crust, whereas the axial volcanism developed in an area that had already become a mid-oceanic ridge setting. Some of the Assab lava flows and spatter cones contain mafic and ultramafic nodules (De Fino et al. 1973). These range from harzburgite and spinel lherzolite to plagioclase peridotite, pyroxenite, and gabbro (Cimmino et al. 1976; Piccardo and Ottonello 1978; Ottonello et al. 1978, 1980). For this study, host basalts and xenoliths were collected from about 5 km NW of the port city of Assab at Mt. El Taghi (Fig. 1). The xenoliths have diameters from ~3 to 9 cm with an average of about 6 cm and all are fresh with no visible alteration in hand specimens or thin sections.

### Analytical procedures

All samples were cut into slabs, trimmed to remove weathered surfaces, and then crushed gently in many stages using a steel mortar and pestle to separate mineral grains from each other while breaking them as little as possible. Whole rock powders of the host basalts and crustal xenoliths were produced in an agate mill. Grains of clinopyroxene, orthopyroxene, olivine, and plagioclase were separated by sieving and hand-picking under a binocular microscope. Before dissolution, clean, visibly inclusion-free mineral grains were washed with cold HCl in an ultrasonic bath, and then repeatedly rinsed with deionized water.

Major and minor elements in the host basalts and crustal xenoliths were analyzed at the University of Bonn by XRF. Typical precisions on major element concentrations are better than 5% and better than 10% for minor and trace elements. Loss on ignition (LOI) values were less than 1.1 wt%. Many samples, however, gained mass during ignition via oxidation of FeO to Fe<sub>2</sub>O<sub>3</sub> and, therefore, have negative LOI values (Table 1). This occurs if the mass

increase as a result of the oxidation of Fe is greater than the mass of OH lost on ignition. Negative LOI values are thus consistent with the absence of OH-bearing alteration minerals in the petrographically fresh host basalts and crustal xenoliths. Furthermore, there is no correlation between LOI and the concentrations of mobile elements such as Rb and K in either the host basalts or crustal xenoliths, suggesting that alteration processes have not affected their chemistry.

For the host basalts and crustal xenoliths, the concentrations of the REE and additional trace elements were determined by inductively coupled plasma mass spectrometry (ICPMS) at ACTlabs, Canada. The analytical data are presented in Table 2 together with the mean values of the international standard BIR-1 obtained during the course of this study.

Major and minor element concentrations in mineral separates were measured using the JEOL JXA8900 electron microprobe at the University of Münster. All minerals were analyzed at 15 kV and 15 nA using a focused beam. Counting times for all elements were 10 s for the peaks and 5 s for the backgrounds except for Na and K, which were counted for 5 and 2.5 s, respectively. All mineral probe analyses presented are averages of three to six individual spots. The analytical data for the minerals are presented in Table 4a (electronic supplementary material).

Trace element concentrations in clinopyroxene, orthopyroxene, and olivine were measured by laser ablation (LA) ICPMS at CODES, University of Tasmania, using a New-Wave Research UP193 Nd-YAG (193 nm) laser coupled to an Agilent 7500cs quadrupole mass spectrometer. Analyses were performed in a He atmosphere by ablating 100 µm diameter spots at a rate of 10 shots/s using a laser power of ~3.5 J/cm<sup>2</sup>. The mass spectrometer was tuned to enhance the sensitivity for mid- to high-mass isotopes (80–240 amu), and to minimize molecular oxide species production by ablating an NIST612 glass. The low level of molecular oxide production (e.g.,  $^{232}\text{Th}^{16}\text{O}^+ / ^{232}\text{Th}^+ < 0.2\%$ ) obviates the need to correct any of the analyte signal intensities for interfering species. Each analysis involves sequential peak hopping through the mass spectrum, with a dwell time of 20 ms on each mass measured. The analysis time for each sample was 90 s, comprising a 30 s background measurement and 60 s analysis with the laser on. Data reduction followed standard methods (Longerich et al. 1996) using the NIST612 glass as a primary reference material and  $^{43}\text{Ca}$  (Ca analyzed by electron microprobe) as the internal standard. The USGS BCR-2 glass was used as a secondary reference material and measured before and after the mineral measurements. The trace element data for minerals are presented in Table 4b (electronic supplementary material) together with mean values of the international standards

**Table 1** Major oxides and trace element abundances of host basalts and crustal xenoliths as determined by XRF

Sample no.: Rock type: Lat. N: Long. E:	Host basalt				Crustal xenolith											
	AE01B/06 Basalt 13°02'00" 42°39'37"	AE04B/06 Basalt 13°01'53" 42°39'43"	AE05B/06 Basalt 13°01'48" 42°39'41"	AE06B/06 Basalt 13°01'46" 42°39'37"	AE07B/06 Basalt 13°01'49" 42°39'29"	AE08B/06 <sup>a</sup> Basalt 13°02'03" 42°39'40"	AE10B/06 <sup>a</sup> Basalt 13°02'03" 42°39'40"	AE12B/06 <sup>a</sup> Basalt 13°02'03" 42°39'40"	AE01A/06 Gabbro 13°02'00" 42°39'37"	AE01C/06 Gabbro 13°02'00" 42°39'37"	AE01D/06 Gabbro 13°02'00" 42°39'37"	AE02/06 Norrite 13°01'58" 42°39'42"	AE04/06 Norrite 13°01'53" 42°39'43"			
Major oxides (wt%)																
SiO <sub>2</sub>	46.1	46.0	46.1	46.8	49.0	48.2	48.2	47.0	48.9	49.9	47.9	52.2	49.1			
TiO <sub>2</sub>	3.10	3.17	3.02	3.01	2.02	2.55	2.56	2.50	0.28	0.53	0.27	1.54	1.15			
Al <sub>2</sub> O <sub>3</sub>	15.5	15.7	15.3	15.7	15.5	15.5	15.6	15.0	16.6	16.9	20.1	17.5	18.9			
Fe <sub>2</sub> O <sub>3</sub> <sup>b</sup>	12.6	12.4	12.7	12.5	10.4	11.1	11.3	11.3	6.69	7.50	6.12	11.0	12.0			
MnO	0.19	0.19	0.18	0.18	0.18	0.19	0.19	0.19	0.11	0.13	0.10	0.19	0.17			
MgO	7.75	7.62	8.08	8.07	6.89	7.41	7.48	8.14	11.5	9.82	10.6	6.65	4.61			
CaO	9.92	9.99	9.98	9.62	9.66	9.71	9.60	9.97	14.0	13.6	13.4	7.18	9.48			
Na <sub>2</sub> O	3.29	3.16	3.12	3.23	3.51	3.21	3.27	2.90	1.66	1.95	2.06	3.59	3.98			
K <sub>2</sub> O	1.09	1.07	0.99	1.05	1.67	1.37	1.38	1.21	0.06	0.11	0.08	0.33	0.20			
P <sub>2</sub> O <sub>5</sub>	0.612	0.608	0.537	0.530	0.601	0.525	0.519	0.500	0.008	0.031	0.014	0.262	0.139			
SO <sub>3</sub>	0.236	0.086	0.584	0.083	0.012	0.024	0.034	0.054	0.012	0.012	0.012	0.160	0.014			
LOI	-0.33	-0.04	0.01	-0.43	0.55	0.05	-0.09	0.84	-0.18	-0.07	-0.25	-0.24	1.07			
Total	100.2	100.2	100.8	100.6	100.2	100.1	100.3	99.9	99.7	100.5	100.5	100.6	100.9			
Trace elements (ppm)																
Sc	27	21	21	25	19	33	14	17	33	33	18	22	26			
V	276	278	289	274	183	249	255	266	124	169	81	249	279			
Cr	200	176	216	220	308	316	309	336	717	537	398	126	55			
Co	42	47	43	40	27	36	47	48	44	40	39	31	32			
Ni	120	111	140	135	118	189	209	234	125	110	159	35	21			
Cu	54	51	63	74	40	108	116	113	3	7	17	23	23			
Zn	96	91	91	101	80	77	85	86	37	47	31	115	78			
Ga	23	24	21	21	17	20	12	17	15	15	10	21	26			
Rb	21	22	18	21	40	36	32	29	2	4	2	2	2			
Sr	545	575	527	536	606	612	601	593	391	414	445	749	768			
Y	36	29	30	31	24	24	23	24	11	11	7	18	10			
Zr	224	229	212	226	283	276	273	275	19	34	21	83	43			
Nb	38	42	39	34	55	57	56	50	2	2	3	15	2			
Ba	316	312	288	328	459	423	413	404	55	115	49	516	168			

<sup>a</sup> Carapace<sup>b</sup> Total iron as Fe<sub>2</sub>O<sub>3</sub>

**Table 2** Trace element abundances of host basalts and crustal xenoliths as determined by ICPMS

Sample no.	AE01B/		AE04B/		AE05B/		AE06B/		AE07B/		AE08B/		AE10B/		AE12B/		AE01A/		AE01C/		AE01D/		AE02/		AE04/		AE06B/		AE10B/		AE10B/		BIR-1	
	06	06	06	06	06	06	06	06	06	06	06 <sup>a</sup>	06	06	06	06	06	06	06	06	06	06	06 <sup>b</sup>	06 <sup>b</sup>	06 <sup>b</sup>	06 <sup>b</sup>	measured	recommended							
V	271	254	257	254	161	212	208	207	122	161	86	228	254	250	214	202	320	313																
Cr	150	140	170	170	210	220	220	250	640	440	330	100	40	170	230	210	390	380																
Co	38	37	38	37	26	32	31	34	40	33	36	22	25	36	32	30	51	51																
Ni	120	110	130	120	90	160	140	180	120	90	140	30	30	110	150	140	170	170																
Cu	40	40	40	50	40	90	90	90	20	20	BD	20	20	60	90	120	130																	
Zn	90	90	90	100	70	70	70	70	40	50	40	100	70	90	70	70	70	70																
Ga	19	19	19	19	15	16	16	16	11	13	12	20	19	19	17	16	16	16																
Rb	20	20	18	19	34	30	28	26	BD	BD	BD	BD	BD	19	29	BD	0.3																	
Sr	499	531	497	507	536	549	547	539	400	394	426	689	690	504	534	109	108																	
Y	31.9	31.8	30.7	31.2	24.9	27.7	27.4	27.0	4.50	8.90	4.10	14.9	6.40	31.3	28.1	26.8	16.0																	
Zr	202	205	190	204	242	250	243	240	7	21	9	58	20	203	249	236	16																	
Nb	35.2	37.6	32.7	34.7	46.8	48.6	47.7	46.9	BD	1.60	0.40	8.30	1.70	34.8	48.9	46.5	0.60																	
Cs	0.2	0.2	0.2	0.2	0.2	0.4	0.3	0.4	BD	BD	BD	BD	BD	0.2	0.3	BD	0.005																	
Ba	328	370	300	328	519	435	441	423	71	103	64	522	209	329	453	429	7																	
La	32.8	32.7	29.4	30.8	45.7	43.3	44.0	42.2	1.23	3.13	1.81	23.0	4.80	31.4	44.4	43.5	0.62																	
Ce	70.8	70.5	63.9	66.5	90.9	89.3	89.8	87.6	3.32	7.24	3.86	41.8	9.20	67.5	90.8	88.7	1.95																	
Pr	8.69	8.82	8.05	8.31	10.5	10.6	10.5	10.4	0.43	1.06	0.53	4.80	1.13	8.42	10.6	10.5	0.38																	
Nd	38.4	38.3	34.8	35.7	40.6	42.7	42.7	42.3	2.16	5.33	2.63	19.5	4.90	36.0	43.2	42.2	2.50																	
Sm	8.43	8.38	7.85	7.93	7.46	8.00	8.19	8.15	0.67	1.49	0.72	3.47	1.09	7.95	8.24	8.14	1.10																	
Eu	2.94	2.92	2.77	2.78	2.47	2.68	2.72	2.72	0.439	0.751	0.471	2.72	1.12	2.77	2.75	2.69	0.540																	
Gd	8.26	8.10	7.91	7.83	6.49	7.13	7.25	7.34	0.87	1.68	0.77	3.16	1.18	7.86	7.36	7.14	1.85																	
Tb	1.31	1.29	1.25	1.25	0.97	1.09	1.10	1.11	0.14	0.29	0.13	0.48	0.20	1.23	1.11	1.10	0.36																	
Dy	7.08	6.89	6.86	6.77	5.27	5.85	5.92	5.93	0.86	1.76	0.82	2.78	1.24	6.74	5.97	5.86	2.50																	
Ho	1.25	1.22	1.22	1.20	0.98	1.08	1.09	1.09	0.17	0.35	0.16	0.57	0.26	1.21	1.09	1.09	0.57																	
Er	3.36	3.32	3.32	3.28	2.70	2.96	3.01	3.02	0.50	1.00	0.46	1.72	0.79	3.29	3.00	3.02	1.70																	
Tm	0.458	0.444	0.449	0.450	0.375	0.407	0.418	0.411	0.069	0.140	0.063	0.262	0.121	0.452	0.420	0.417	0.260																	
Yb	2.76	2.68	2.69	2.72	2.32	2.47	2.53	2.50	0.40	0.85	0.39	1.80	0.83	2.74	2.58	2.47	1.65																	
Lu	0.387	0.381	0.386	0.386	0.352	0.363	0.374	0.370	0.056	0.126	0.059	0.289	0.134	0.392	0.370	0.377	0.260																	
Hf	5.2	5.3	5.1	5.3	6.0	6.1	6.1	6.1	0.30	0.80	0.30	1.6	0.60	5.3	6.2	6.1	0.60																	
Ta	2.87	2.99	2.62	2.73	3.88	3.82	3.88	3.82	0.01	0.08	0.02	0.49	0.11	2.72	3.93	3.84	0.04																	
Pb	BD	BD	BD	7	BD	BD	BD	BD	BD	BD	BD	30	BD	7	BD	BD	3																	
Th	2.61	2.67	2.46	2.62	4.41	4.06	4.10	4.10	0.05	0.12	BD	0.23	0.08	2.61	4.15	4.05	0.03																	
U	0.88	0.84	0.81	0.87	0.90	1.20	1.20	1.19	0.05	0.07	0.06	0.16	0.10	0.86	1.21	1.19	0.01																	

BD below detection limit

<sup>a</sup> Carapace

<sup>b</sup> Duplicate analysis

BCR-2 obtained during the course of this study. All analyses were normalized to the recommended values of BCR-2.

The concentrations of Sm, Nd, Rb, and Sr as well as the isotope compositions of Nd and Sr were determined by isotope dilution TIMS at the Institut für Mineralogie, University of Münster. Neodymium and Sr measurements were normalized to  $^{146}\text{Nd}/^{144}\text{Nd} = 0.7219$  and  $^{86}\text{Sr}/^{88}\text{Sr} = 0.1194$ , respectively, using the exponential law. La Jolla Nd and NBS-987 Sr standards measured during the course of this study yielded mean values of  $0.511861 \pm 17$  (2SE,  $n = 12$ ) and  $0.710244 \pm 37$  (2SE,  $n = 9$ ), for  $^{143}\text{Nd}/^{144}\text{Nd}$  and  $^{87}\text{Sr}/^{86}\text{Sr}$ , respectively. Lutetium and Hf concentrations as well as the isotopic composition of Hf were determined by MC-ICPMS at the Institut für Mineralogie, University of Münster. Hafnium isotopic ratios were normalized to  $^{179}\text{Hf}/^{177}\text{Hf} = 0.7325$  using the exponential law and are reported relative to  $^{176}\text{Hf}/^{177}\text{Hf} = 0.282163$  for the JMC-475 standard. The 2SD external reproducibility of  $^{176}\text{Hf}/^{177}\text{Hf}$  for unknowns was estimated from the relationship between the external (2SD) reproducibility and internal run statistics (2SE) of standards analyzed at a variety of signal intensities (see Bizzarro et al. 2003). This resulted in the relationship  $2\text{SD} (\text{external}) = \sim 2.3 \times 2\text{SE} (\text{internal})$ . For isotope dilution measurements of Lu concentrations, the  $^{176}\text{Lu}/^{175}\text{Lu}$  values were corrected for  $^{176}\text{Yb}$  interference and mass bias using the naturally occurring Yb in the samples (Blichert-Toft et al. 2002).

All isotope data for host basalts, crustal xenoliths, and mineral separates of mantle xenoliths are presented in Table 3. Epsilon parameters ( $\epsilon_{\text{Nd}}$  and  $\epsilon_{\text{Hf}}$ ) were calculated relative to the CHUR parameters of Bouvier et al. (2008, i.e.,  $^{143}\text{Nd}/^{144}\text{Nd} = 0.512630$  and  $^{176}\text{Hf}/^{177}\text{Hf} = 0.282785$ ).

### Mineralogy and equilibration temperatures and pressures

#### Host basalts

The host basalts are fine-grained, vesicular, and porphyritic with olivine (Fo<sub>77–86</sub>), plagioclase (An<sub>56–67</sub>), and diopsidic clinopyroxene (Mg# 69–79; Table 4a) phenocrysts set in a groundmass of plagioclase, pyroxene, olivine, and opaque phases. They also show pilotaxitic and glomero-porphyritic textures. The host basaltic carapaces adhering to mantle xenoliths (i.e., the thin skins of basalt which encrust xenolith samples AE08B, 10B, 12B, 18B, and 20B) are very fine-grained, vesicular, and vitrophyric with microphenocrysts of dominantly plagioclase and olivine with minor clinopyroxene. They also show pilotaxitic texture. Most samples also contain plagioclase and pyroxene xenocrysts.

#### Crustal xenoliths

The crustal xenoliths are coarse-grained, layered, granular olivine gabbros (samples AE01A, C, and D) containing olivine (Fo<sub>72–79</sub>), orthopyroxene (Mg# 72–78), diopsidic clinopyroxene (Mg# 76–81), and plagioclase (An<sub>65–71</sub>), and norites (samples AE02 and 04) containing olivine (Fo<sub>69</sub>), orthopyroxene (Mg# 60–62), and plagioclase (An<sub>45</sub>; Table 4a).

#### Mantle xenoliths

The ultramafic xenoliths contain a primary assemblage of ol + opx + cpx + sp ± pl; no hydrous minerals were observed. The 15 investigated xenoliths were subdivided into four groups on the basis of their mineralogy: dunite (AE13, 19, and 20: olivine > 90%; orthopyroxene + clinopyroxene + spinel < 10%), spinel lherzolite (AE08, 09, 10, 12, 18, and 21: olivine 45–65%, orthopyroxene 7–15%, clinopyroxene 25–35%, and spinel < 7%), plagioclase-free pyroxenite (AE14, 15, and 16: olivine 5–10%, orthopyroxene 20–45%, clinopyroxene 50–70%, and spinel < 5%) and plagioclase–spinel pyroxenite (AE11, 17, and 22: olivine 12–25%, orthopyroxene 20–30%, clinopyroxene 40–50%, spinel < 15%, and plagioclase 3–10%). These rocks are dominantly protogranular, characterized by coarse olivine and pyroxene grains, and rarely equigranular. Weak porphyroclastic texture is observed in some samples as manifested by kink bands in olivine and rare aggregates of several olivine crystals having similar orientation that were likely produced by recrystallization of larger olivine grains. All minerals occur as anhedral or (rarely) euhedral crystals and show no alteration. Grain boundaries are usually curvilinear except where localized recrystallization has produced polygonal mineral grains having straight boundaries that meet at 120°. The clinopyroxene in the plagioclase–spinel pyroxenites is leaf green (in hand specimen) whereas in the other xenoliths it is emerald green and sometimes displays exsolution lamellae. Diffuse to well-defined clinopyroxene-rich layers (bands) are commonly observed. Spinel typically occurs as small grains at grain boundaries as anhedral (vermicular) interstitial crystals and as inclusions. In the plagioclase–spinel pyroxenites, spinel also occurs as worm-like, cuneiform grains in pyroxene. Furthermore, euhedral (samples AE19 and 17) and poikilitic (sample AE12) spinel grains are found in the dunites, spinel lherzolites, and plagioclase–spinel pyroxenites. The color of spinel ranges from reddish-brown in the dunites to brown in the lherzolites and plagioclase-free pyroxenites, to green in plagioclase–spinel pyroxenites, with some grains having opaque rims. Thin, spinel-rich layers are observed in some samples. Symplectitic intergrowths of

**Table 3** Sr–Nd–Hf isotope data for host basalts, crustal and mantle xenoliths

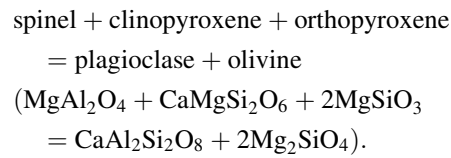
Sample no.	Sm (ppm)	Nd (ppm)	$^{147}\text{Sm}/^{144}\text{Nd}$	$^{143}\text{Nd}/^{144}\text{Nd}$	$\epsilon_{\text{Nd}}^a$	Rb (ppm)	Sr (ppm)	$^{87}\text{Rb}/^{86}\text{Sr}$	$^{87}\text{Sr}/^{86}\text{Sr}$	Lu (ppm)	Hf (ppm)	$^{176}\text{Lu}/^{177}\text{Hf}$	$^{176}\text{Hf}/^{177}\text{Hf}$	$\epsilon_{\text{Hf}}^a$
<b>Host basalt</b>														
AE01B/06				0.512987(5)	7.0				0.703358(7)				0.283080(4)	10.4
AE04B/06				0.512985(3)	6.9				0.703431(7)				0.283079(4)	10.4
AE05B/06				0.512986(4)	6.9				0.703492(9)				0.283087(3)	10.7
AE06B/06				0.512978(2)	6.8				0.703382(7)				0.283083(4)	10.5
AE07B/06				0.512983(4)	6.9				0.703517(9)				0.283087(4)	10.7
AE08B/06				0.512974(3)	6.7				0.703411(6)				0.283069(3)	10.0
AE10B/06				0.512977(6)	6.8				0.703489(10)				0.283076(3)	10.3
AE12B/06				0.512967(2)	6.6				0.703563(7)				0.283067(4)	10.0
<b>Crustal xenolith</b>														
AE01A/06	0.615	2.01	0.1851	0.512687(8)	1.1	0.261	420	0.0018	0.704374(14)	0.057	0.279	0.0291	0.282905(13)	4.2
AE01C/06	1.29	4.55	0.1714	0.512667(7)	0.7	0.894	418	0.0062	0.704951(16)	0.118	0.689	0.0243	0.282923(7)	4.9
AE01D/06	0.622	2.25	0.1674	0.512759(9)	2.5	0.431	448	0.0028	0.704519(13)	0.053	0.374	0.0201	0.282897(13)	4.0
AE02/06	3.16	17.3	0.1108	0.512213(10)	−8.1	0.525	752	0.0020	0.707906(13)	0.259	1.56	0.0236	0.282489(6)	−10.5
AE04/06	1.02	4.42	0.1390	0.512711(6)	1.6	0.874	764	0.0033	0.704977(14)	0.121	0.614	0.0280	0.282807(21)	0.8
<b>Mantle xenolith</b>														
<b>Clinopyroxene</b>														
AE08/06	0.998	2.74	0.2202	0.512928(29)	5.8				0.703444(8)	0.158	0.504	0.0445	0.283116(8)	11.7
AE09/06	0.846	1.80	0.2842	0.512947(7)	6.2				0.703805(6)	0.174	0.401	0.0615	0.283197(9)	14.6
				0.512943(31)	6.1				0.703839(14)					
AE10/06	0.900	2.44	0.2234	0.512930(31)	5.9				0.703448(8)	0.153	0.398	0.0546	0.283112(12)	11.6
AE11/06	0.760	2.41	0.1907	0.512882(18)	4.9				0.704048(8)	0.091	0.487	0.0265	0.283107(14)	11.4
AE14/06	0.722	1.80	0.2422	0.512911(15)	5.5				0.703694(9)	0.127	0.304	0.0594	0.283136(12)	12.4
AE15/06	0.538	0.924	0.3521	0.512950(12)	6.2				0.703774(7)	0.130	0.213	0.0868	0.283258(12)	16.7
				0.513042(5)	8.0				0.703733(35)					
AE16/06	0.698	1.48	0.2860	0.513042(5)	8.0				0.703104(5)	0.140	0.275	0.0725	0.283349(10)	19.9
				0.513050(49)	8.2				0.703140(11)					
AE17/06	0.885	1.93	0.2777	0.512855(26)	4.4				0.704091(8)	0.128	0.249	0.0726	0.283105(11)	11.3
AE18/06	1.16	2.80	0.2505	0.512897(9)	5.2				0.703963(6)					
AE19/06	0.897	2.98	0.1822	0.512880(8)	4.9				0.703371(7)	0.099	0.360	0.0389	0.283156(9)	13.1
				0.512863(21)	4.6									
AE20/06	0.643	1.30	0.2987	0.512950(11)	6.2				0.703644(7)	0.166	0.244	0.0965	0.283273(10)	17.3
AE21/06	1.07	2.56	0.2534	0.512859(7)	4.5				0.703978(7)	0.126	0.513	0.0349	0.283073(10)	10.2
<b>Orthopyroxene</b>														
AE14/06									0.705827(15)	0.034	0.036	0.1359	0.283200(24)	14.7
AE15/06										0.038	0.027	0.1989	0.283262(24)	16.9

Table 3 continued

Sample no.	Sm (ppm)	Nd (ppm)	$^{147}\text{Sm}/^{144}\text{Nd}$	$^{143}\text{Nd}/^{144}\text{Nd}$	$\epsilon_{\text{Nd}}^a$	Rb (ppm)	Sr (ppm)	$^{87}\text{Rb}/^{86}\text{Sr}$	$^{87}\text{Sr}/^{86}\text{Sr}$	Lu (ppm)	Hf (ppm)	$^{176}\text{Lu}/^{177}\text{Hf}$	$^{176}\text{Hf}/^{177}\text{Hf}$	$\epsilon_{\text{Hf}}^a$
AE16/06									0.703856(15)	0.043	0.043	0.1408	0.283274(19)	17.3
Plagioclase														
AE11/06									0.704031(10)					
AE17/06									0.704066(8)					
AE22/06									0.703998(6)					

<sup>a</sup>  $\epsilon_{\text{Nd}}$  and  $\epsilon_{\text{Hf}}$  are calculated relative to the CHUR parameters of Bouvier et al. (2008, i.e.,  $^{143}\text{Nd}/^{144}\text{Nd} = 0.512630$  and  $^{176}\text{Hf}/^{177}\text{Hf} = 0.282785$ )

spinel and plagioclase are common in the plagioclase–spinel pyroxenites, suggesting a decompression reaction:



In most samples, sponge-like textures are observed in spinel and pyroxene, and sometimes in olivine as well. In addition, trace amounts of plagioclase occur as discrete reaction products both in the dunites and lherzolites. Veins and pockets of silicate and carbonate (former) melts containing crystals of olivine, plagioclase, carbonate, and opaque phases  $\pm$  pyroxene are also common in most samples.

Equilibration temperatures calculated using the two-pyroxene thermometer of Brey and Köhler (1990) range from 870 to 1,040°C (Table 4a; Fig. 2). No well-constrained geobarometers exist for the estimation of equilibration pressures in spinel peridotites or pyroxenites. This is due to the lack of suitable equilibria associated with a high volume change. However, several authors have attempted to calibrate single-phase geobarometers that are mainly based on clinopyroxene compositions. So far, these are the only way to independently estimate equilibration pressures in spinel facies ultramafic rocks. The 0.8–2.0 GPa pressures calculated using the clinopyroxene barometer of Mercier (1980) are only approximations of relative

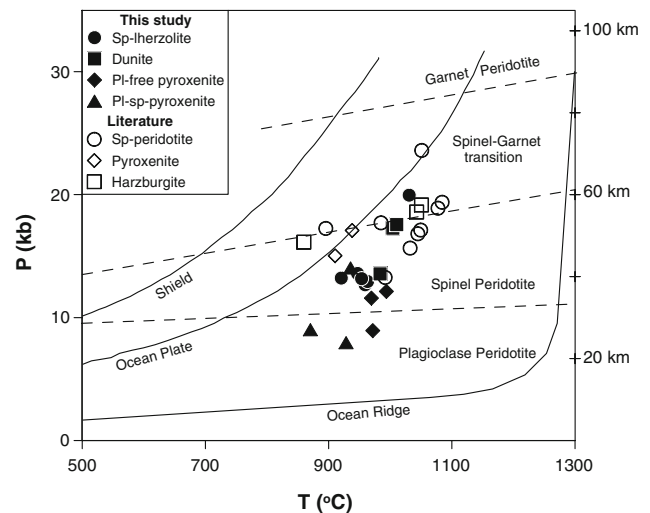


**Fig. 2** Estimated  $P$ – $T$  of equilibration for the Assab peridotites and pyroxenites using the two-pyroxene thermometer of Brey and Köhler (1990) and the single clinopyroxene geobarometer of Mercier (1980). Geotherms and peridotite transitions are from Wylie (1981) and McGuire (1988 and references therein). Sources of data for Assab: Cimmino et al. (1976), Piccardo and Ottonello (1978), Ottonello et al. (1978, 1980)

equilibration pressures (Table 4a; Fig. 2). Nevertheless, this barometer does yield relatively lower pressures for the plagioclase–spinel pyroxenites as compared to the lherzolites and dunites, which is petrologically reasonable. Furthermore, the estimation of equilibration pressures for the Assab xenoliths by fitting to the ocean plate geotherm of Wylie (1981), which is in agreement with the tectonic environment of the Afar Depression being transitional between continental rifting and sea floor spreading, gave similar results; i.e., the plagioclase–spinel pyroxenites equilibrated at lower pressures as compared to the lherzolites and dunites.

## Results

### Major and trace elements

#### Host basalts

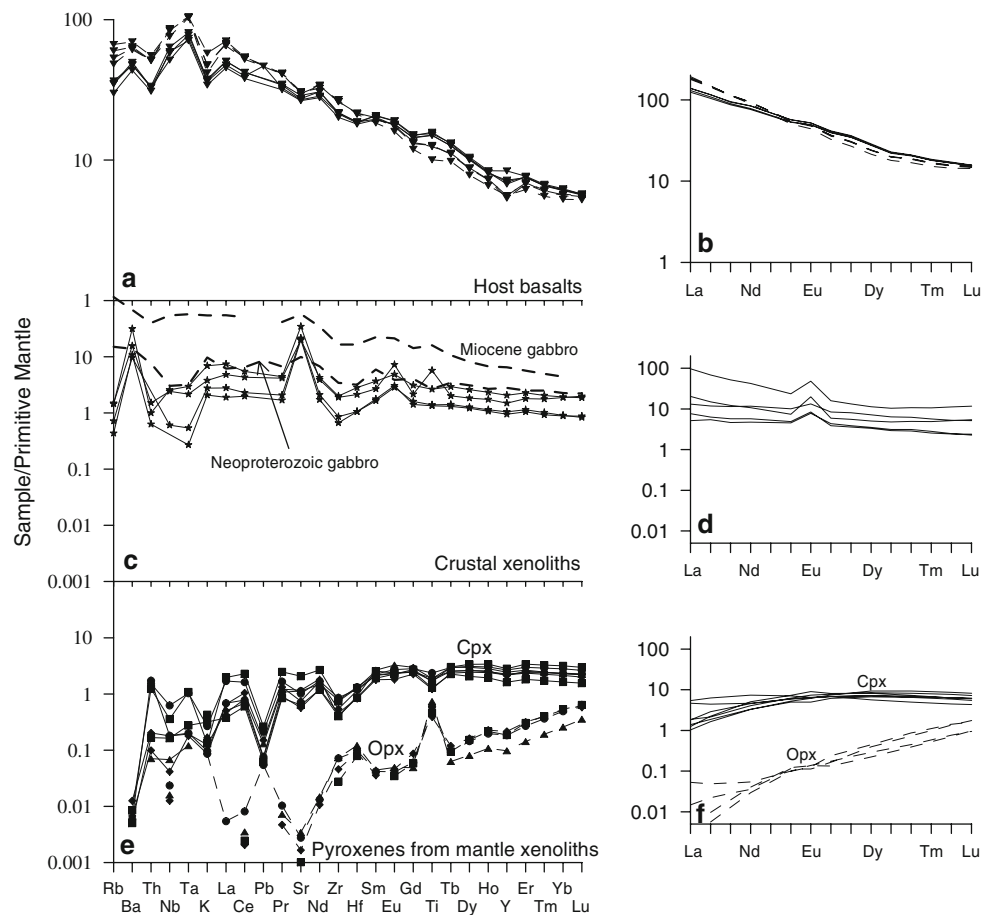
All analyzed host lavas are nepheline-normative alkaline basalts and show a narrow compositional variability suggesting that the degree of fractional crystallization among the basalts was limited. The basalts contain 7–8 wt% MgO,

10–13 wt% Fe<sub>2</sub>O<sub>3</sub> (total, all Fe calculated as Fe<sup>3+</sup>), ~15.5 wt% Al<sub>2</sub>O<sub>3</sub>, ~9.8 wt% CaO, and ~3.3 wt% Na<sub>2</sub>O (Table 1). These host basalts have a low Mg# (0.58–0.61), and low Ni (111–234 ppm) and Cr (176–336 ppm) contents, suggesting that they underwent fractional crystallization before eruption and are therefore not primary melts. The relatively wider ranges in Ni, Cr, and Sc (Table 1) and the decrease of CaO/Al<sub>2</sub>O<sub>3</sub> with decreasing MgO indicate the importance of olivine, clinopyroxene, and plagioclase fractionation in producing the small amount of compositional variation observed among the basalts.

Primitive mantle-normalized multi-element and REE patterns for the host basalts are shown in Fig. 3a. All basalts display enriched REE patterns, (Ce/Yb)<sub>N</sub> ranging from 6.2 to 10.3, and very slight positive Eu-anomalies (1.07–1.08). All samples are characterized by strong enrichment in the most highly incompatible elements coupled with enrichments of the moderately incompatible elements relative to HREE and Y.

The Sr–Nd–Hf isotope ratios of the host basalts are quite similar (Table 3) and there is no increase in Sr or decrease in Nd or Hf isotope ratios with decreasing Mg# that would be expected in rocks affected by crustal contamination. Hence, in these rocks, ratios of incompatible elements

**Fig. 3** Primitive mantle-normalized multi-element (a, c, e) and chondrite-normalized REE (b, d, f) patterns for the Assab host basalts (basaltic carapaces and sample AE07B/06, *dashed lines*; a, b), crustal xenoliths and representative Neoproterozoic and Miocene gabbros (*dashed lines*; c, d) from Eritrea and Yemen, respectively (Teklay et al. 2001; Chazot and Bertrand 1993), and clinopyroxene (*solid lines*) and orthopyroxene (*dashed lines*) from mantle xenoliths (e, f). Normalizing values are from McDonough and Sun (1995)



having similar distribution coefficients should reflect the source characteristics and the magmatic processes that have affected the host basalts. Detailed observations of the host basalts show the presence of two groups (Tables 1, 2; Fig. 3a, b). The basaltic carapaces (AE08B, 10B, and 12B) and sample AE07B are relatively more alkaline (higher  $\text{Na}_2\text{O} + \text{K}_2\text{O}$ ) and, for a given MgO content, show higher abundances in all incompatible elements except Ti, Y, and HREE (Tables 1, 2; Fig. 3a). They also tend to have higher Mg#, Cr, and Ni contents. However, the ratios of highly incompatible elements that have crystal/melt partition coefficients close to 0 (e.g., Ba/Nb, Ba/La, Nb/La, Nb/Th, and Cs/Rb) that are not likely to be modified by partial melting and fractional crystallization processes are similar for both groups (Tables 1, 2; Fig. 3a). These, together with the similar Sr–Nd–Hf isotope ratios, suggest the same homogenous source for both groups. On the other hand, ratios of highly to moderately incompatible elements (e.g., La/Yb, Nb/Zr, Nb/Y, Ba/Zr), which are modified during partial melting but not during typical degrees of fractional crystallization, differ between the two groups, suggesting a variable degree or depth of melting. The high values of these ratios [e.g.,  $(\text{Ce}/\text{Yb})_{\text{N}} = 9.2\text{--}10.3$  vs.  $6.2\text{--}6.9$ ] in combination with relatively lower Y and HREE abundances for the basaltic carapaces (AE08B, 10B, and 12B) and sample AE07B suggest that these samples have been formed by relatively lower degrees of partial melting or at greater depth.

#### Crustal xenoliths

The three gabbro xenoliths (AE01A, C, and D) have similar chemical compositions:  $\sim 10.5$  wt% MgO,  $\sim 13.5$  wt% CaO,  $\sim 6.8$  wt%  $\text{Fe}_2\text{O}_3$  (total), low  $\text{TiO}_2$  (0.2–0.5%), slightly enriched REE patterns,  $(\text{Ce}/\text{Yb})_{\text{N}}$  between 2.2 and 2.6, and positive Eu-anomalies (1.45–1.93; Fig. 3b, d). The two norite xenoliths (AE02 and 04) have higher  $\text{TiO}_2$  ( $\sim 1.3$  wt%),  $\sim 11.5$  wt%  $\text{Fe}_2\text{O}_3$  (total), and lower MgO ( $< 7$  wt%) and CaO ( $\sim 8$  wt%). They also have relatively enriched REE patterns, with  $(\text{Ce}/\text{Yb})_{\text{N}}$  ranging from 2.9 to 6.1, and pronounced positive Eu-anomalies (2.5–3.0). In addition to their departures from smooth curves, the spidergrams for the gabbroic crustal rocks show marked depletions in the high field strength elements (HFSE: e.g., Zr, Hf, Ta, Nb), Th, and U and high LREE/HFSE. Furthermore, their relative enrichments in large ion lithophile elements (LILE: e.g., Ba, Sr, Pb) lead to positive anomalies and high values in LILE/HFSE and LILE/LREE (Fig. 3b).

#### Mantle xenoliths

Bulk compositions of mantle xenoliths may provide valuable constraints on the nature of the lithospheric mantle,

but this record can be overprinted by a range of processes that contribute conflicting geochemical signatures to an individual xenolith. We avoided these possible complications by analyzing core compositions of large clear grains to evaluate the primary mineralogy of the lithosphere under the Assab region. The cores are remarkably homogeneous and separate grains from a single rock sample are homogenous within the analytical error, indicating the absence of post-crystallization reactions between minerals and melt in the analyzed grains.

**Olivine.** The forsterite content of olivine ranges from  $\text{Fo}_{92}$  in the dunites to  $\text{Fo}_{79}$  in the plagioclase–spinel pyroxenites. Nickel, Cr, and V correlate positively with— and Co and Mn correlate negatively with— forsterite content (Tables 4a, b; Fig. 4). Furthermore, equilibration temperatures also correlate positively with the forsterite content of olivine (Fig. 4). The concentrations of most incompatible trace elements in olivine are below detection limits (Table 4b).

**Orthopyroxene.** The Mg# of orthopyroxene ranges from 80 in the plagioclase–spinel pyroxenites to 91 in the dunites. The proportions of enstatite correlate positively with forsterite content of the co-existing olivine (Fig. 4). Nickel, Cr, and Sc correlate positively with— and Ti, Al, Co, and Mn correlate negatively with—the Mg# of the orthopyroxene (Tables 4a, b; Fig. 5). Furthermore, equilibration temperatures also correlate positively with Mg#. Orthopyroxene from all xenolith types shows depleted REE patterns, with  $(\text{Ce}/\text{Yb})_{\text{N}}$  ranging from 0.004 to 0.063 (Fig. 3f). Primitive mantle-normalized multi-element patterns of the orthopyroxene separates are shown in Fig. 3e. Positive K and Ti anomalies and negative Sr anomalies are evident in Fig. 3e.

**Clinopyroxene.** The clinopyroxene is Al–Cr–diopside with 0.28–1.56 wt%  $\text{Cr}_2\text{O}_3$ , 3.15–6.83 wt%  $\text{Al}_2\text{O}_3$ , 0.10–0.84 wt%  $\text{TiO}_2$ , and 0.38–0.91 wt%  $\text{Na}_2\text{O}$ . The Mg# ranges from 81 to 92 and correlates positively with the forsterite content of co-existing olivine and the Mg# of co-existing orthopyroxene (Table 4a; Fig. 4). As with the orthopyroxene, the clinopyroxene in the dunites has a higher Mg#, higher  $\text{Cr}_2\text{O}_3$ , and lower  $\text{Al}_2\text{O}_3$ ,  $\text{Na}_2\text{O}$ , and  $\text{TiO}_2$  than in the other xenolith types (Table 4a; Fig. 5). The clinopyroxene predominantly has depleted chondrite-normalized REE patterns, with  $(\text{Ce}/\text{Yb})_{\text{N}}$  ranging from 0.19 to 0.69 (Fig. 3f). Only clinopyroxene from samples AE11 and AE19 shows slightly enriched REE patterns, with  $(\text{Ce}/\text{Yb})_{\text{N}}$  values of 1.10 and 1.41, respectively. Primitive mantle-normalized multi-element patterns for the clinopyroxene are shown in Fig. 3e where negative anomalies for Ba, Nb, K, Pb, Sr, Zr, and Ti are evident.

**Spinel.** The Mg# of spinel ranges from 59 to 73 and correlates with the forsterite content of the co-existing olivine and the Mg# of the co-existing ortho- and clinopyroxene

**Fig. 4** NiO, equilibration T, Cr, and Mg# of clinopyroxene, orthopyroxene, and spinel versus forsterite content of co-existing olivine. Sources of data as in Fig. 2

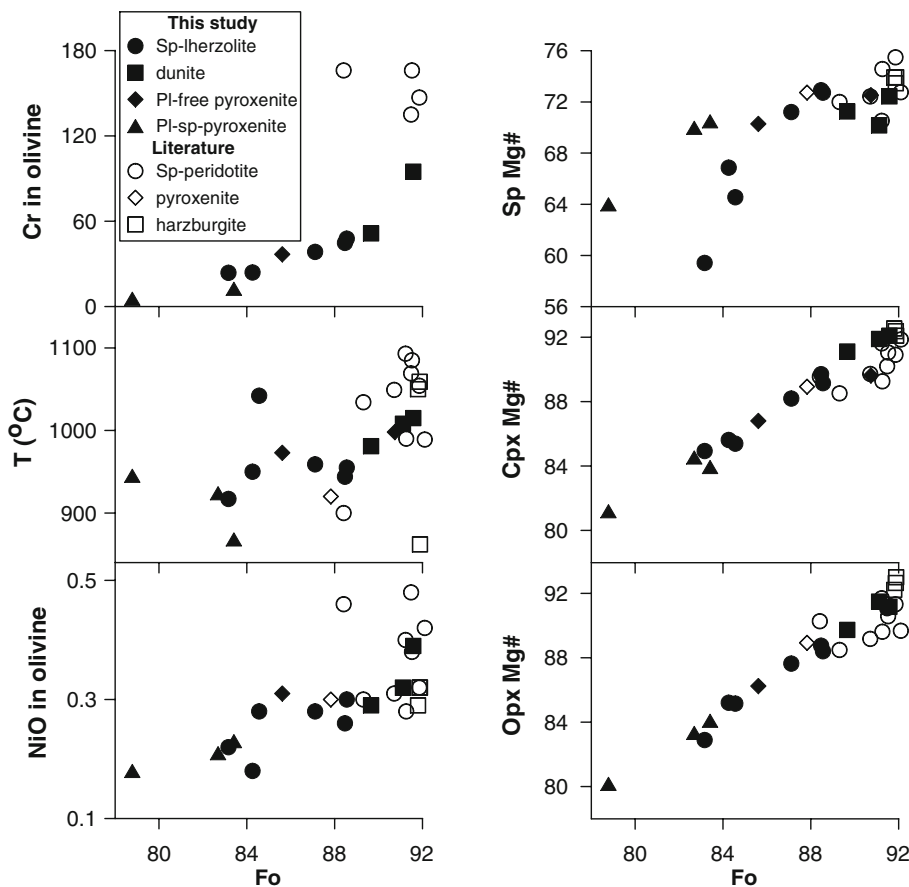


**Fig. 5** Clinopyroxene (left) and orthopyroxene (right)  $Al_2O_3$ , and  $Cr_2O_3$  versus Mg#. Symbols and sources of data as in Fig. 4

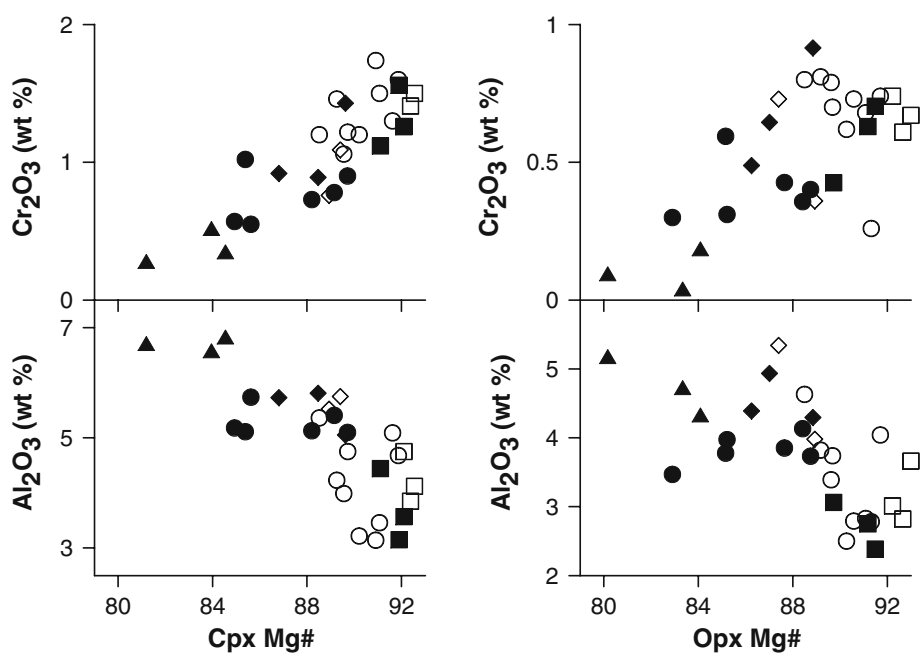


(Table 4a; Fig. 4). The reddish-brown spinel in the dunites is  $Cr_2O_3$ -rich (26.4–40.4 wt%) and  $Al_2O_3$ -poor (27.3–42.0 wt%), the green spinel in the plagioclase–spinel pyroxenites is  $Cr_2O_3$ -poor (0.8–5.7 wt%) and  $Al_2O_3$ -rich

(59.0–64.5 wt%), and the brown spinel in the lherzolites and plagioclase-free pyroxenites has intermediate compositions (Table 4a). Hence, the spinels in the four types of xenoliths can be distinguished from each other by color and Cr#.

**Plagioclase.** The anorthite content of the plagioclase in the spinel–plagioclase pyroxenites ranges from An<sub>64</sub> to An<sub>81</sub>. The anorthite content of the plagioclase that occurs as a discrete reaction product in the lherzolites (e.g., sample AE09 = An<sub>78</sub>) also lies within this range (Table 4a).

### Sr–Nd–Hf isotope ratios

The Sr–Nd–Hf isotope ratios of host basalts, crustal xenoliths, and mineral separates from the mantle xenoliths (clinopyroxene, orthopyroxene, and plagioclase) are given in Table 3 and shown in Figs. 6 and 7. The host basalts all have similar Sr–Nd–Hf isotope ratios:  $^{87}\text{Sr}/^{86}\text{Sr} = 0.70336\text{--}0.70356$ ,  $\epsilon_{\text{Nd}} = +6.6$  to  $+7.0$ , and  $\epsilon_{\text{Hf}} = +10.0$  to  $+10.7$  (Fig. 6). Clinopyroxene from mantle xenoliths displays a limited range in isotope composition:  $^{87}\text{Sr}/^{86}\text{Sr} = 0.70310\text{--}0.70409$ ,  $\epsilon_{\text{Nd}} = +4.4$  to  $+8.0$ , and  $\epsilon_{\text{Hf}} = +10.2$  to  $+19.9$  (Fig. 7). Orthopyroxene from the plagioclase-free pyroxenites has  $^{87}\text{Sr}/^{86}\text{Sr} = 0.70386\text{--}0.70583$  and  $\epsilon_{\text{Hf}} = +14.7$  to  $+17.3$ , and the plagioclase from the plagioclase–spinel pyroxenites has  $^{87}\text{Sr}/^{86}\text{Sr} = 0.70400\text{--}0.70407$  (Table 3). In contrast, the gabbroic crustal xenoliths show wider ranges:  $^{87}\text{Sr}/^{86}\text{Sr} = 0.70437\text{--}0.70791$ ,  $\epsilon_{\text{Nd}} = -8.1$  to  $+2.5$ , and  $\epsilon_{\text{Hf}} = -10.5$  to  $+4.9$  (Table 3; Fig. 6). The clinopyroxene separates from the Assab mantle xenoliths are compatible with 30 Ma Sm–Nd and Lu–Hf reference lines (Fig. 8). This is the time of plume impingement on the base of the lithosphere in this region. In contrast, the whole rock gabbros (crustal xenoliths) spread along steeper, Neoproterozoic reference lines (Fig. 8).

### Discussion

#### Host basalts

Quaternary volcanism in the Afar Depression is manifested mainly as two distinct types of volcanic structures. One is characterized by axial ranges that display topographic, seismic, and gravimetric similarities to mid-oceanic spreading ridges. These volcanic units, which are less than a million years old, are typically produced by basaltic fissure eruptions occurring along NW–WNW-aligned axes. The other type of volcanic structure is characterized by ranges that are transverse to the main tectonic trend of the depression. These are marked by alignments of scoria cones and basaltic flows along an E–W to NE–SW direction, and include the Assab range and the islands of Hanish and Zubair (Fig. 1). These transverse volcanic structures are considered to be the equivalents of oceanic fracture zones and are contemporaneous with volcanism at the axial ranges (Barberi and Varet 1977). It is well documented that

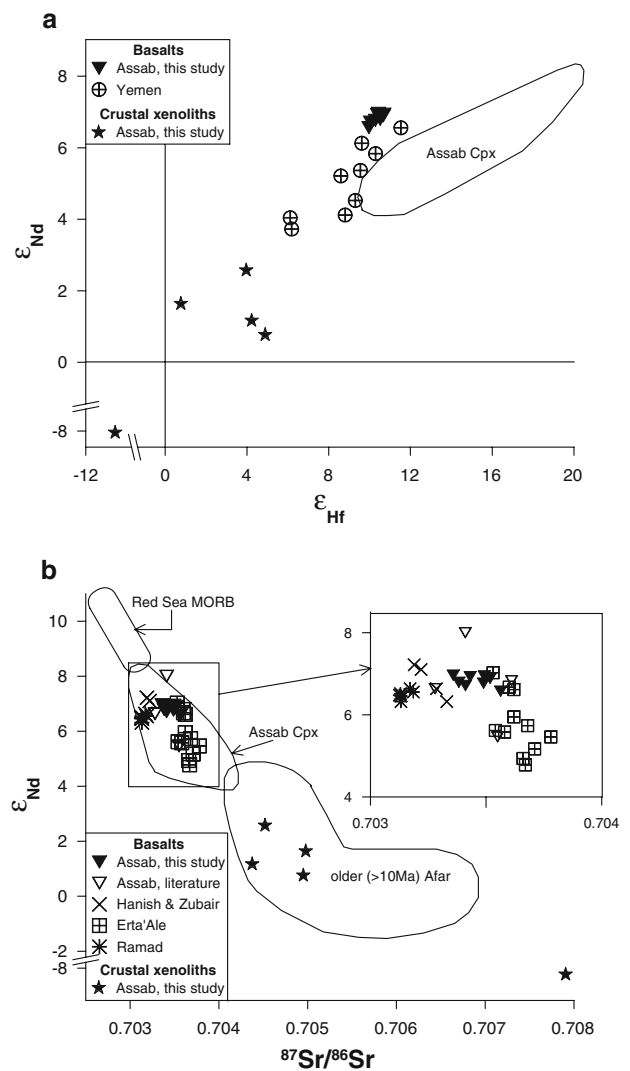


**Fig. 6** Sr–Nd–Hf isotope data for the Assab host basalts and crustal xenoliths compared to basalts from the Afar volcanic province. Sources of data: Assab (Barberi et al. 1980; Betton and Civetta 1984), Hanish and Zubair islands (Volker et al. 1997), Erta’ Ale (Barrat et al. 1998), Ramad sea mount (Volker et al. 1997), Yemen (Bertrand et al. 2003), and fields for 19°–23°N Red Sea MORB (<http://www.petdb.org/>), older Afar basalts (>10 Ma, i.e., Mabla and older basalts, Barrat et al. 1993; Deniel et al. 1994), and Assab clinopyroxene (this study). Note the breaks in the axes

the transverse tectonic structures of the Afar Depression are characterized by alkaline basaltic volcanism that contrasts with the transitional basaltic volcanism of the axial ranges (De Fino et al. 1973; Barberi et al. 1974; Civetta et al. 1975). Basalts from the transverse tectonic structures have the highest abundances of most highly incompatible trace elements, suggesting that they were derived by a lower degree of melting than the axial range basalts (Fig. 9a). Geochemical variations in the Afar Depression (axial ranges and transverse volcanic structures) have been variously interpreted to reflect derivation from a vertically

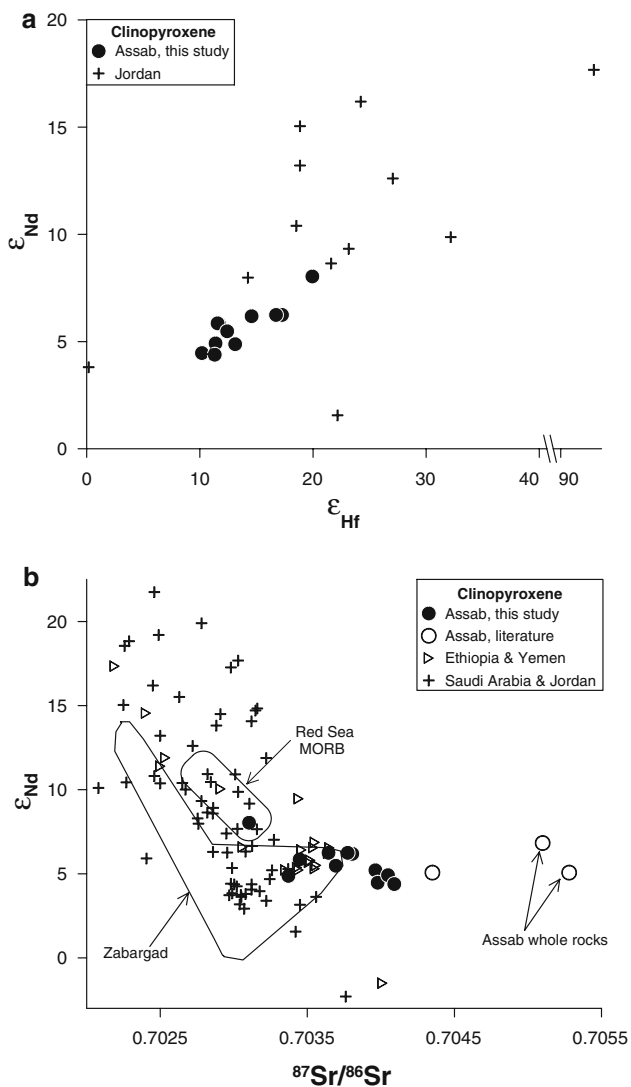


**Fig. 7** Sr–Nd–Hf isotope data for clinopyroxene from Assab peridotites and pyroxenites. For comparison, data are shown for clinopyroxene from other xenoliths: Assab (Betton and Civetta 1984) and the two whole rock spinel peridotites with the highest Sr isotope ratios from Ottonello et al. 1978), Ethiopia (Roger et al. 1999), Jordan (Shaw et al. 2007), Saudi Arabia (Henjes-Kunst et al. 1990; Blusztajn et al. 1995), Yemen (Baker et al. 2002), and Zabargad island (Brueckner et al. 1988)

zoned mantle source (Barberi et al. 1980; Betton and Civetta 1984), and to be the result of mixing between the depleted Red Sea MORB source and an enriched plume source (Hart et al. 1989; Schilling et al. 1992; Barrat et al. 1998).

Figure 6 presents the Sr–Nd isotope compositions of basalts having >5 wt% MgO from the Assab region, Erta’Ale, and the islands of Hanish and Zubair (in the southern Red Sea axial trough), together with typical Red Sea N-MORB (19°–23°N), and the Ramad enriched component. The Assab host basalts have Sr–Nd isotope values

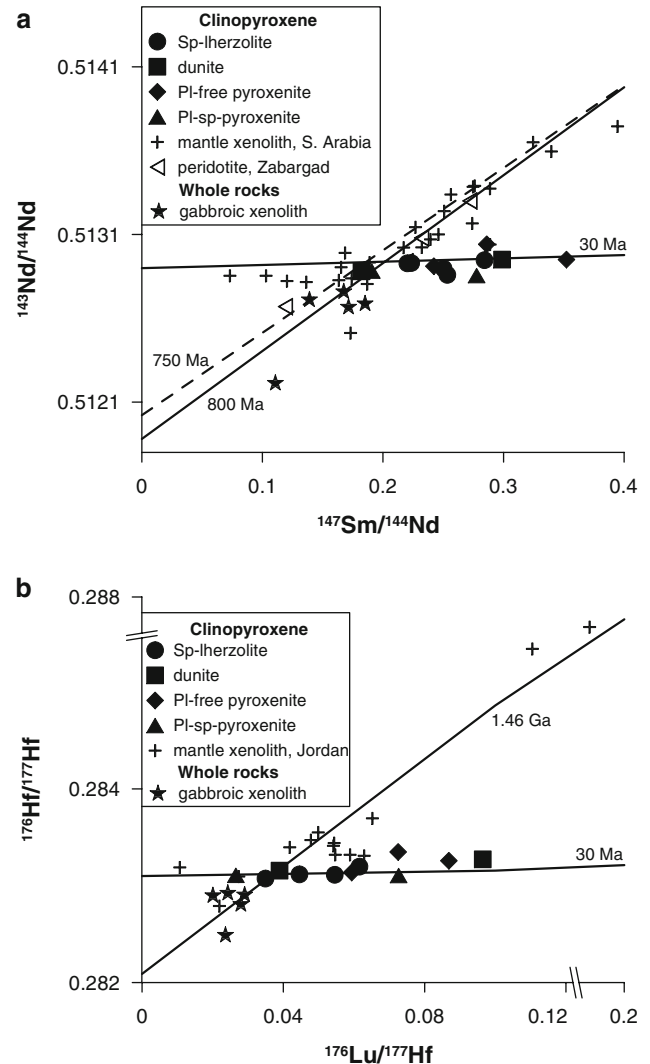
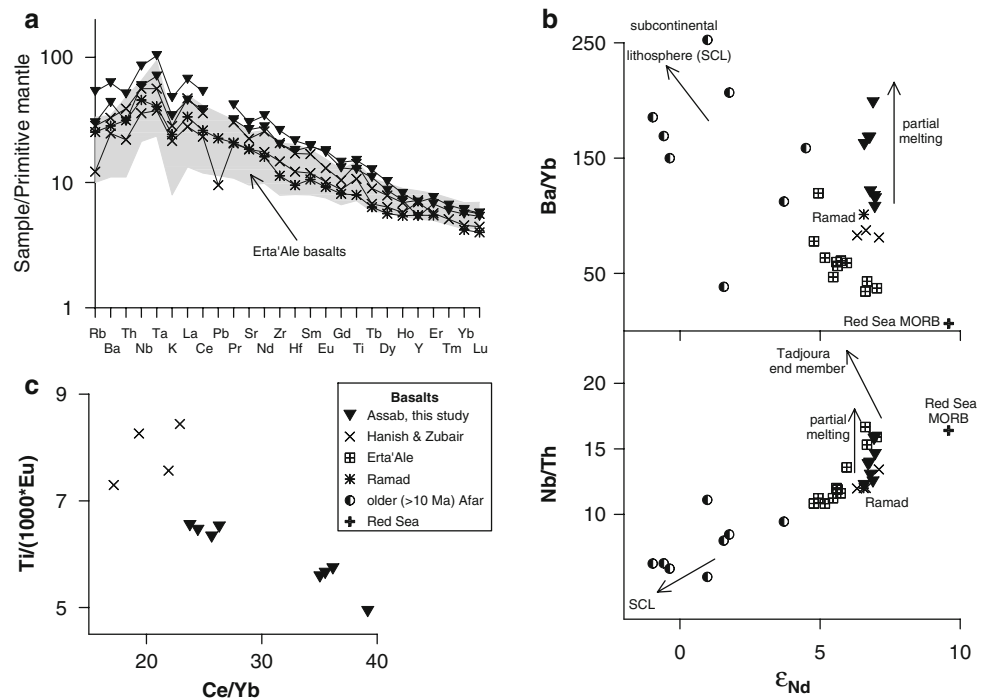


**Fig. 8** Sm–Nd (a) and Lu–Hf (b) isochron diagrams showing Assab crustal gabbroic xenoliths and clinopyroxene separates from mantle xenoliths in relation to clinopyroxene separates from mantle xenoliths from Saudi Arabia (Henjes-Kunst et al. 1990) and Jordan (Shaw et al. 2007), and Zabargad island peridotites (Brueckner et al. 1988). The Assab mantle xenoliths plot near ~30 Ma reference lines, whereas the crustal gabbroic xenoliths and the other mantle xenoliths and peridotites from the region plot near Proterozoic reference lines (e.g., ~0.75–0.80 Ga for the Sm–Nd system or ~1.5 Ga for the Lu–Hf system)

that are similar to those of the Hanish and Zubair basalts, and they also have trace element patterns that parallel those of the Hanish and Zubair basalts despite having slightly higher abundances of the most highly incompatible elements due to a lower degree of melting (Fig. 9a). Basalts from the transverse tectonic structures, including the Assab host basalts, and basalts from Hanish and Zubair islands have somewhat more depleted Sr–Nd isotope values as compared to basalts from the axial ranges, i.e., the Erta’Ale basalts (Fig. 6). Figure 9b clearly shows that neither the Assab host basalts nor the basalts from Hanish and Zubair

**Fig. 9** **a** Trace element patterns, **b** Nb/Th and Ba/Yb versus epsilon Nd, and Ti/Eu versus Ce/Yb for Assab host basalts as compared to basalts from Ramad seamount, Erta'Ale, and islands of Hanish and Zubair. Basalts from Assab and islands of Hanish and Zubair plot close to the enriched Ramad and do not extend into the fields for older (>10 Ma) Afar or Tadjoura basalts, whereas the Erta'Ale basalts extend to the field of the older Afar basalts that is dominated with a significant contribution from a subcontinental lithosphere. Symbols and sources of data as in Fig. 6



islands require a contribution from a third component that dominates the older (>10 Ma) Afar basalts or a contribution from the Tadjoura component. Hence, the Assab host basalts, like the basalts from the Hanish and Zubair islands, seem to be predominantly derived from melting of the enriched Ramad mantle component.

The two distinct types of volcanic structures in the Afar Depression, the axial ranges and the transverse volcanic structures, are related in space and time. However, they show different melting conditions and isotopic characteristics. The basalts of the transverse volcanic structures are characterized by depleted Sr and Nd isotopic signatures, and by either lower degrees of melting or greater depths of melting. In contrast, the basalts of the axial ranges have relatively enriched Sr and Nd isotopic signatures and likely originated by melting at shallow depth or by greater extents of melting. We suggest that both are from the same Afar mantle source as represented by the Ramad seamount, but some basalts of the axial ranges have been more contaminated by the high  $^{87}\text{Sr}/^{86}\text{Sr}$  and low  $^{143}\text{Nd}/^{144}\text{Nd}$  subcontinental lithosphere (Fig. 9a, b).

A closer inspection of the Sr isotope variations of the Assab host basalts and basalts from the islands of Hanish and Zubair (Fig. 6b, inset) shows a trend toward higher  $^{87}\text{Sr}/^{86}\text{Sr}$  values at similar  $^{143}\text{Nd}/^{144}\text{Nd}$  values for the Assab host basalts. These rocks also trend towards higher Ce/Yb and lower Ti/Eu (Fig. 9c). The criteria proposed by Rudnick et al. (1993) for recognition of the signature of carbonate-related metasomatism include high LREE/HREE, very high Zr/Hf and very low Ti/Eu. Thus, the

higher Sr isotope ratios measured in the Assab host basalts may indicate that their source has been more affected by carbonate-related metasomatism than the source of the Hanish and Zubair basalts.

#### Gabbroic xenoliths

The crustal xenoliths show the largest variation in Sr–Nd–Hf isotope ratios. Their  $^{87}\text{Sr}/^{86}\text{Sr}$  ranges from 0.70437 to 0.70791,  $\epsilon_{\text{Nd}}$  from  $-8.3$  to  $+2.4$ , and  $\epsilon_{\text{Hf}}$  from  $-10.0$  to  $+5.3$ . They have trace element characteristics and primitive mantle-normalized geochemical patterns similar to those of the Neoproterozoic rocks of the Arabian–Nubian Shield and modern arc rocks. These similarities include enrichment in LILE and depletion in HFSE (Figs. 3c, 10). Furthermore, their high La/Nb values ( $\sim 2$ – $4.5$ ; Fig. 10) and low Ni contents ( $<35$  ppm) at a Mg# of 40 suggest that the gabbroic xenoliths are subduction-related cumulates (Condie 1999). On Sm–Nd and Lu–Hf isochron diagrams, the crustal xenoliths plot near Proterozoic trends defined by mantle xenolith clinopyroxene separates from the broader region (e.g., Jordan, Saudi Arabia, Yemen, Ethiopia, and Egypt; Fig. 8). Hence, we interpret the Assab mafic lower crustal xenoliths to be part of the Neoproterozoic subduction-related cumulates of the Arabian–Nubian Shield (Teklay 2006).

#### Mantle xenoliths

On the basis of major element systematics of bulk samples, the compositional trends of the peridotitic mantle xenoliths

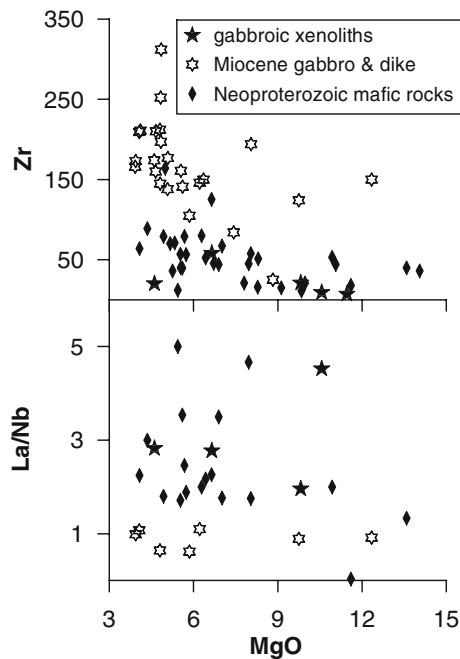


**Fig. 10** Zr and La/Nb versus MgO for gabbroic xenoliths as compared to Neoproterozoic mafic arc rocks from Eritrea (Teklay 2006 and references therein) and Miocene gabbro and dikes from Yemen and Saudi Arabia (Capaldi et al. 1987; McGuire and Coleman 1986; Manetti et al. 1991; Chazot and Bertrand 1993)

have been mostly ascribed to effects of progressive partial melting. For example, the Assab xenoliths have been interpreted to represent residues after various degrees of partial melting (Ottonello et al. 1978; Ottonello 1980). However, as we will explain below, the wide range in the composition of the different minerals in the Assab ultramafic rocks is more suggestive of fractional crystallization processes than partial melting processes. As a consequence, the Assab ultramafic rocks are probably not mantle residues but may rather be sequences of layered cumulates from a relatively enriched picritic melt.

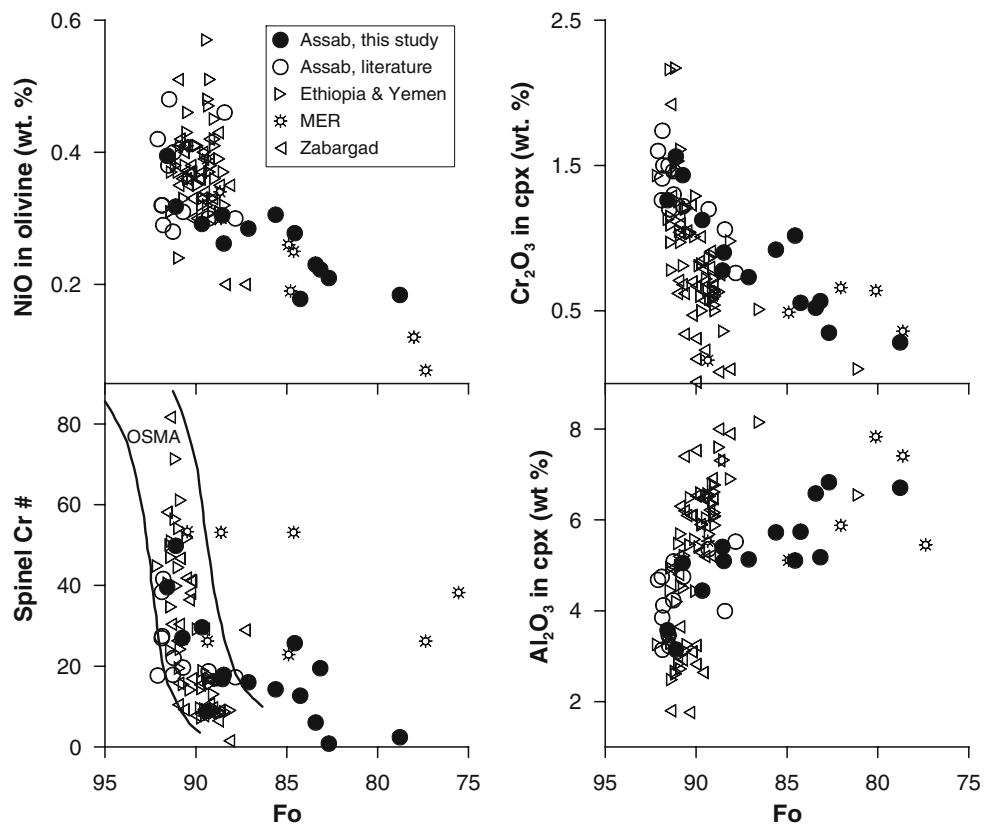
The Mg# of peridotitic mantle olivine is between 88 and 92 and reflects that of the whole rock, which in turn is related to the degree of melt depletion or enrichment. Xenoliths that crystallized from silicate melts are generally Fe-enriched relative to depleted peridotite and hence their olivine has a lower Mg# (Pearson et al. 2004 and references therein). The olivine in the Assab peridotites and pyroxenites ranges down to lower forsterite content (Fo<sub>79–92</sub>) suggesting that the rocks are crystallization products of silicate melts. Likewise, the Mg#s of orthopyroxene and clinopyroxene in mantle peridotites are typically above 90, suggestive of their residual character. In contrast, the Mg#s of orthopyroxene and clinopyroxene of the Assab xenoliths extend to lower values and vary widely from 80 to 91 and from 81 to 92, respectively.

Figure 11 is a plot of spinel Cr# versus the forsterite content of co-existing olivine showing the olivine–spinel mantle array (OSMA), which was argued by Arai (1994) to be residual in nature. The Assab xenoliths, which plot outside this array toward lower Fo values, are therefore apparently not mantle residues but rather a suite of cumulates. This is further supported by the presence of clinopyroxene- and spinel-rich layers and euhedral spinel crystals in the Assab xenoliths, which constitute structural and textural evidence for accumulation and crystallization from a melt. Note that several xenoliths from the Main Ethiopian Rift (Rooney et al. 2005) also plot to the low-Fo side of OSMA in Fig. 11 and these may be cumulates as well.

Trends in the abundance of compatible transition elements can also be utilized to test cumulate and residue hypotheses. Elements having bulk solid/liquid partition coefficients of 2–10 do not vary much in the residue during (fractional) fusion, whereas fractional crystallization can cause significant abundance changes in cumulates. There are large ranges in compatible element abundances in the minerals of the Assab xenoliths. For example, Cr contents vary by a factor of 4 in olivine (0.26–0.94 wt%), by a factor of 8 in orthopyroxene (0.046–0.35 wt%) and by a factor of 19 in clinopyroxene (5–95 ppm). Within these ranges, Cr contents are in agreement with their corresponding Mg# and largely reflect the amount of fractional crystallization that had already taken place in the melt(s) before the cumulate peridotites and pyroxenites crystallized from them (Tables 4a, b; Fig. 11).

The Mg# of olivine, clinopyroxene, and orthopyroxene, the Cr# of spinel, and the abundances of compatible elements progressively increase with increasing temperature of xenolith equilibration and also relatively with increasing pressure (Tables 4a, b). Such variations are compatible with the Assab xenoliths being sequences of cumulates whose layering was controlled by the order of appearance of the cumulus phases and their relative density. Fractional crystallization and accumulation gave rise to the following main lithotypes: dunite, spinel lherzolite, plagioclase-free pyroxenite, and plagioclase–spinel pyroxenite. The Assab dunites, presumably the early peridotite cumulates, have high-Fo olivine, high Mg# in clinopyroxene and orthopyroxene, and high Cr# in spinel, high compatible element contents (e.g., Ni, Cr), and relatively high average *P* and *T* of equilibration. These values generally decrease from dunites through spinel lherzolites to plagioclase–spinel pyroxenites (from early to late cumulates), as is typical for rocks related by differentiation (fractional crystallization) processes. The dunites are apparently derived from the least fractionated liquids, so their olivine, pyroxenes, and spinel have compositions similar to those of their

**Fig. 11** Spinel Cr# and NiO of olivine and  $\text{Al}_2\text{O}_3$  and  $\text{Cr}_2\text{O}_3$  of co-existing clinopyroxene versus forsterite content in olivine. The Assab mantle xenoliths are compared with those from Ethiopia and Yemen xenoliths, and the Zabargad peridotites. Sources of data: Ethiopia (Bedini et al. 1997; Bedini and Bodinier 1999; Conticelli et al. 1999; Roger et al. 1999; Orlando et al. 2006; Ferrando et al. 2007), Main Ethiopian Rift (MER, Rooney et al. 2005), Yemen (Chazot et al. 1996), Zabargad (Bonatti et al. 1986; Piccardo et al. 1988; Kurat et al. 1993). Olivine–spinel mantle array (OSMA) is from Arai (1994)



counterparts in dunite and harzburgite residues that remain after partial melting of mantle peridotite.

In anhydrous spinel peridotites, clinopyroxene is the main carrier of REE, Ti, and Zr (Pearson et al. 2004 and references therein). Recognizing that clinopyroxene dominates the bulk distribution coefficients of incompatible elements in anhydrous spinel peridotites, the REE in Assab xenoliths can be used to model fractional crystallization (Fig. 12). Accordingly, about 10–60% of fractional crystallization was needed to form the Assab-layered cumulates (Fig. 12). The results of the crystallization models are illustrative but are not unique. Some xenoliths do have stronger LREE (La and Ce) enrichment than predicted by the model. These xenoliths also show higher Pb, Th, U, and Nb contents and trend towards higher Zr/Hf, La/Zr, and La/Ti values (Tables 4a, b; Fig. 13). These enrichments and trends are not related to the fractional crystallization process, but most likely reflect cryptic metasomatic enrichment in some xenoliths. Carbonate-related metasomatism causes a relative enrichment in LREE and Sr over HREE and HFSE leading to high LREE/HFSE values (Ionov et al. 1993; Ionov 1998). Given the presence of carbonate veins and melt pockets in the samples, the xenoliths that show enrichment in LREE may have been affected by carbonate-related metasomatism. The distinctly higher  $^{87}\text{Sr}/^{86}\text{Sr}$  ratios of whole rock samples of the Assab spinel peridotites

compared to clinopyroxene separates at similar  $\epsilon_{\text{Nd}}$  values (Fig. 7) have also been interpreted to result from carbonate-related metasomatism (Otonello et al. 1978).

The limited variation of the Sr–Nd–Hf isotope ratios among the clinopyroxene separates and their correlation of these ratios with the degree of fractionation (Mg# of olivine, clinopyroxene, and orthopyroxene), abundances of compatible elements (Fig. 14), and compatible-to-incompatible element ratios suggest that the Assab cumulates were genetically related and formed relatively recently (<50 Ma). For both Lu–Hf and Sm–Nd systems, the Assab cumulates form general trends that are consistent with 30 Ma reference lines (Fig. 8). This time marks the onset of magmatic activity that was triggered by the impingement of the Afar plume head on the lithosphere of this region (e.g., Hoffman et al. 1997). The initial  $^{143}\text{Nd}/^{144}\text{Nd}$  and  $^{176}\text{Hf}/^{177}\text{Hf}$  of the reference lines (i.e., ca. +6 and +12 epsilon units, respectively) are suggestive of a source that was somewhat enriched relative to the average MORB source mantle.

Mantle xenolith suites often sample the mantle over a range of pressure and temperature, and because they are transported to the surface with little or no re-equilibration, they are very useful for estimating lithospheric thickness and geothermal gradients (e.g., Rudnick et al. 1998), and in some cases provide evidence for a vertical stratigraphy

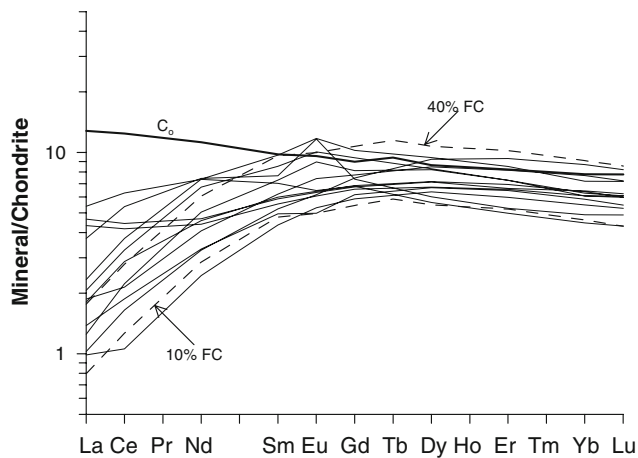


**Fig. 12** Model fractional crystallization (*instantaneous solid*) of an enriched source (*dashed lines*) as compared to REE data from Assab clinopyroxene separates showing that the Assab peridotites and pyroxenites could be formed as cumulates from such a source. The source,  $C_0$ , is 20% batch melting of a primitive mantle composition (McDonough and Sun 1995) with a starting and melt modes of 0.55 and 0.10 for olivine, 0.25 and 0.20 for orthopyroxene, 0.18 and 0.68 for clinopyroxene, and 0.02 and 0.02 for spinel, after Johnson et al. (1990). Equation for instantaneous solid:  $C_{\text{cpx}} = C_0 D_{\text{cpx}} F^{(X_{\text{cpx}} \times D_{\text{cpx}} - 1)}$ , where  $X_{\text{cpx}} = 0.3$ . Partition coefficients are taken from Rollinson (1993)

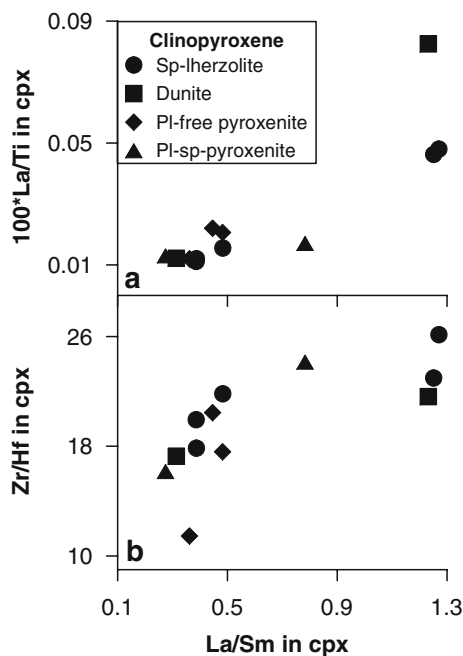


**Fig. 13** La/Ti and Zr/Hf versus La/Sm for Assab clinopyroxenes

(e.g., Griffin et al. 1999). The  $P$ – $T$  estimates for the Assab xenoliths (Fig. 2) scatter near the ocean plate geotherm of Wylie (1981) at higher temperatures than those expected in continental shield geotherms and at lower temperatures than those expected in ocean ridges. This is in agreement with the tectonic environment of the Afar Depression being

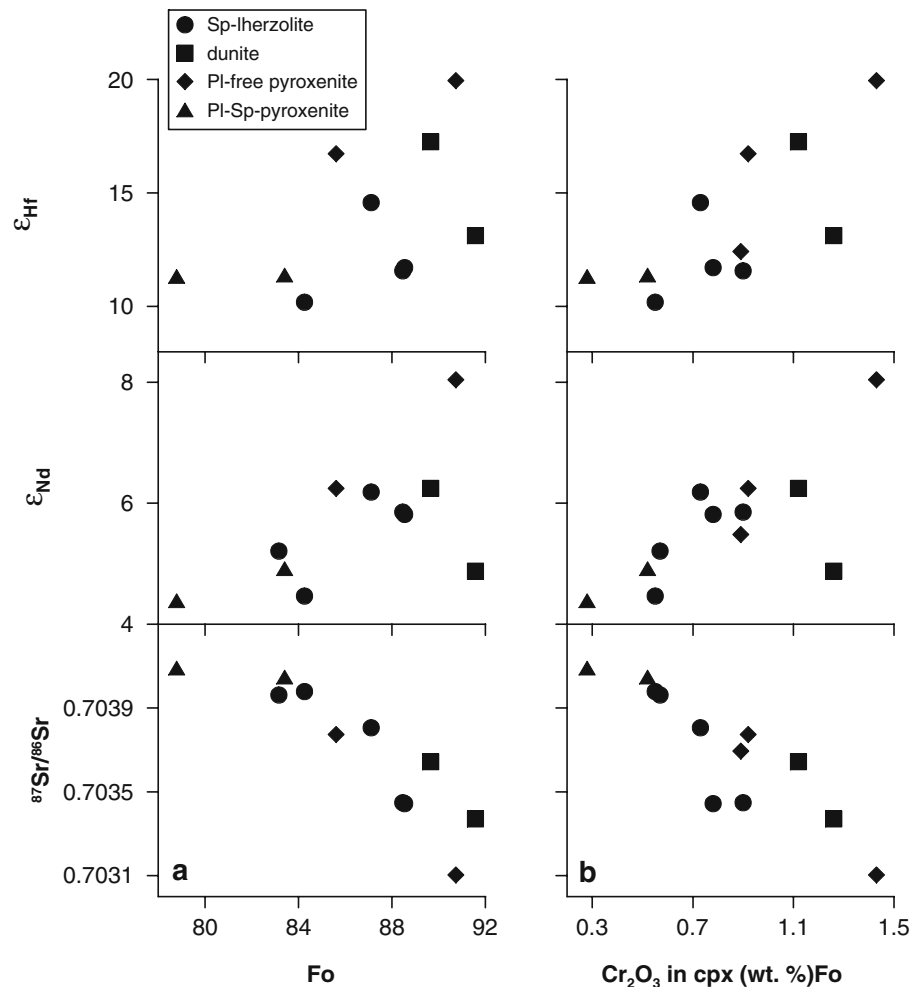
transitional between continental rifting and sea floor spreading. The higher temperature of the upper mantle material under the Afar is also supported by the results of the magnetotelluric soundings of this area (Berkbold et al. 1975).

The crustal structure of the Afar Depression and East African rift as obtained from seismic and gravity data departs from that of typical continental crust in both thickness and velocity distribution in the crust and upper mantle. Seismic (e.g., Makris and Ginzburg 1987; Dugda et al. 2005) and gravity (e.g., Makris and Ginzburg 1987; Tiberi et al. 2005) studies within the Red Sea, Afar, and the Main Ethiopian Rift suggest that the crust beneath the Main Ethiopian Rift and the Afar Depression is continental in nature, but thinned, being thickest ( $\sim 40$  km) under the plateau, and thinner ( $\sim 32$  km) under the Main Ethiopian Rift. The latter crust thins toward the north in the Afar Depression to  $\sim 25$  km. This thickness of the Afar crust as determined by geophysical methods is similar to the geobarometric estimate for the depth of origin of the Assab plagioclase–spinel pyroxenites (Fig. 2).

In the Afar Depression, the thinned crust is underlain by an upper mantle having an abnormally low velocity of 7.4 km/s, which has been interpreted to indicate the presence of a large intrusive complex there. Inferred densities of 3.0–3.1 g/cc suggest that this complex most likely consists of mantle or a mixture of crust and mantle material (Makris and Ginzburg 1987). Tiberi et al. (2005) have interpreted the higher Bouguer gravity values over the Afar region as being caused by a thin (23 km) and dense crust that was modified by magmatic underplating at the crust–mantle boundary. In the western plateau of Ethiopia, a 15-km-thick layer having a velocity of 7.4 km/s beneath the crust has been interpreted as evidence for magmatic underplating during the Oligocene and/or the Holocene (MacKenzie et al. 2005).

These unusual velocity and gravity characteristics of the crust and upper mantle under the Main Ethiopian Rift and the Afar Depression are most likely a result of the tremendous amount of mafic dykes and sills that make up the crust in this area (e.g., Makris and Ginzburg 1987; MacKenzie et al. 2005; Tiberi et al. 2005). Such unusual seismic velocities ( $V_p = 7.3$ – $7.8$  km/s) at the base of the crust are observed in both continental and oceanic environments. In continental settings, these layers are associated with rift volcanism and are generally interpreted as large, underplated igneous intrusions emplaced before or during rifting (e.g., Farnetani et al. 1996). Furthermore, in provinces affected by plume magmatism, the largest volumes of volcanic rocks are tholeiitic basalts that have lower MgO concentrations indicating the significant degree of crystal fractionation they have undergone before being erupted. In contrast to their occurrence in oceanic

**Fig. 14** Sr–Nd–Hf isotope ratios versus forsterite content of olivine (a) and Cr<sub>2</sub>O<sub>3</sub> content of clinopyroxene (b) for Assab mantle xenoliths



environments, picrites are very rare in continental flood basalt provinces, suggesting the great importance of the hidden cumulates in the lower crust and upper mantle compositions of the continental lithosphere. Farnetani et al. (1996) suggested the high-velocity layers beneath oceanic plateaus and hot spot tracks represent fractionated cumulates from picritic mantle melts and are therefore an integral part of plume magmatism. The chemical compositions of the Assab xenoliths are consistent with such an origin and thus these rocks may represent cumulates that crystallized from deep, picritic melts of the Afar plume.

A schematic cross-section of the lithosphere under Afar Depression presented in Fig. 15 summarizes the important conclusions derived from the study of Assab xenoliths. Taken together, the Assab xenoliths' compositions and estimated  $P$ – $T$  of origin together with existing geophysical data all suggest that the lithosphere below the Afar Depression consists of an upper crust of lavas, sediment cover, and Neoproterozoic granitic rocks, underlain by a Neoproterozoic mafic igneous lower crust and an upper mantle with cumulate layers and melt.

## Conclusions

A detailed geochemical and isotopic study of gabbroic, peridotitic, and pyroxenitic xenoliths and their host basalts from the Assab area, Afar Depression provides important insights into the geodynamic evolution of a rift system, and constrains important aspects of the rifting process, including the local geothermal gradient. The main conclusions of this study can be summarized as follows.

The alkaline host basalts show enriched REE patterns and trace element geochemical characteristics similar to those of ocean island basalts. The basalts define limited ranges in Sr–Nd–Hf isotope ratios that do not correlate with fractionation index, indicating the absence of significant crustal contamination. On the other hand, correlations between isotope and trace element ratios provide evidence for the interaction of the Afar plume and the depleted Red Sea MORB mantle source in the petrogenesis of these host basalts.

The gabbroic crustal xenoliths have the highest  $^{87}\text{Sr}/^{86}\text{Sr}$  values and the lowest  $\epsilon_{\text{Nd}}$  and  $\epsilon_{\text{Hf}}$ . They have trace element

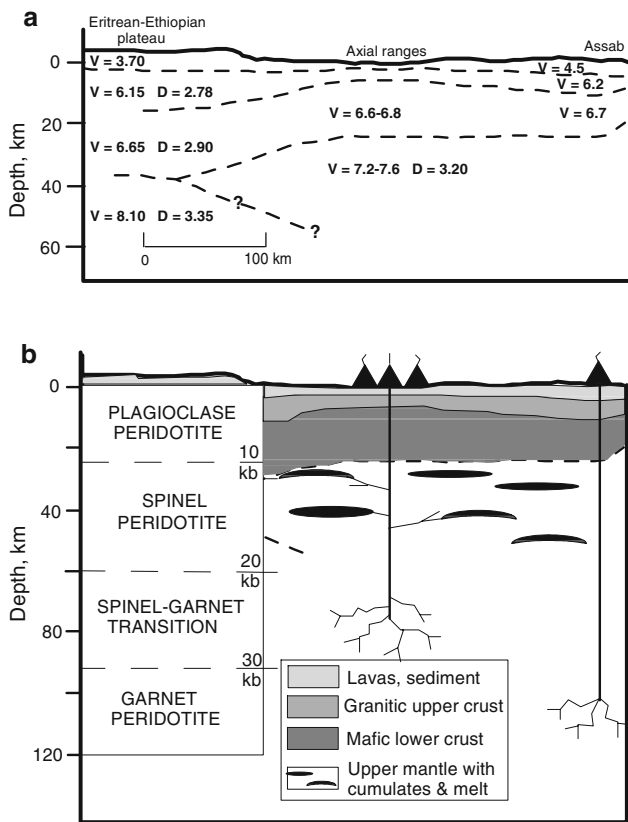


**Fig. 15** Seismic data (**a**) and schematic cross-section of the upper lithosphere beneath Afar Depression (**b**). Seismic data are from Ottonello et al. (1978) and the left-hand column showing peridotite phase relations is from McGuire (1988 and references therein)

characteristics that are similar to those of rocks from the Neoproterozoic Arabian–Nubian Shield and modern arcs, i.e., enrichment in the LILE (e.g., Ba, Sr, and Pb) and marked depletions in the HFSE (e.g., Zr, Hf, and Nb). Hence, the lower crust of the Afar Depression is inferred to comprise mostly Neoproterozoic mafic igneous rocks.

The Assab ultramafic xenoliths are not products of crystallization of their host magmas. Rather, they apparently crystallized from an earlier generation of similar magmas. The xenoliths show systematic chemical variations that largely reflect the relative degree of fractional crystallization that their parental melts had already undergone. The fractional crystallization resulted in the formation of layered sequences of cumulates from a relatively enriched, Afar plume-derived, originally picritic melt. The  $P$ – $T$  estimates for the xenoliths from the Assab region follow a steeper geothermal gradient than that expected for continental shields, consistent with the tectonic environment of the Afar Depression. The Assab mantle xenoliths provide strong evidence for the presence of significant amounts of hidden cumulate rock within the lower crust and upper mantle of the continental lithosphere and

account for the rare occurrence of picrites as compared to tholeiitic basalts in continental flood basalt provinces.

**Acknowledgments** This study was conducted while M. Teklay was a recipient of fellowships from the Alexander von Humboldt Stiftung (Georg Forster) and the Deutsche Forschungsgemeinschaft. We kindly acknowledge H. Baier and J. Berndt for their assistance in the laboratory, TIMS, and microprobe analyses, and J. Blundy and S. Klemme for their fruitful discussions. Ruesom Teclamarium is thanked for his support in Assab during sample collection. Finally, we thank Jean-Alix Barrat and an anonymous reviewer, whose insightful comments helped improve the manuscript.

**Open Access** This article is distributed under the terms of the Creative Commons Attribution Noncommercial License which permits any noncommercial use, distribution, and reproduction in any medium, provided the original author(s) and source are credited.

## References

- Arai S (1994) Characterization of spinel peridotites by olivine–spinel compositional relationships: review and interpretation. *Chem Geol* 113:191–204
- Audin L, Quidelleur X, Coulié E, Courtillot V, Gilder S, Manighetti I, Gillot PY, Tapponnier P, Kidane T (2004) Palaeomagnetism and K–Ar and  $^{40}\text{Ar}/^{39}\text{Ar}$  ages in the Ali Sabieh area (Republic of Djibouti and Ethiopia): constraints on the mechanism of Aden ridge propagation into southeastern Afar during the last 10 Myr. *Geophys J Int* 158:327–345. doi:10.1111/j.1365-246X.2004.02286.x
- Baker J, Chazot G, Menzies M, Thirlwall M (2002) Lithospheric mantle beneath Arabia: a Pan-African protolith modified by the afar and older plumes, rather than a source for continental flood volcanism? In: Menzies MA, Klemperer SL, Ebinger CJ, Baker JA (eds) *Volcanic rifted margins*. *Geol Soc Am Spec Paper* 362, pp 65–80
- Barberi F, Varet J (1977) Volcanism of Afar: small scale plate tectonic implications. *Geol Soc Am Bull* 88:1251–1266
- Barberi F, Bonatti E, Marinelli G, Varet J (1974) Transverse tectonics during the split of a continent: data from the Afar rift. *Tectonophysics* 23:17–29
- Barberi F, Civetta L, Varet J (1980) Sr isotopic composition of Afar volcanics and its implication for mantle evolution. *Earth Planet Sci Lett* 50:247–259
- Barrat JA, Jahn BM, Fourcade S, Joron JL (1993) Magma genesis in an ongoing rifting zone: The Tadjoura Gulf (Afar area). *Geochim Cosmochim Acta* 57:2291–2302
- Barrat JA, Fourcade S, Jahn BM, Cheminée JL, Capdevila R (1998) Isotope (Sr, Nd, Pb, O) and trace-element geochemistry of volcanics from the Erta’Ale range (Ethiopia). *J Volcanol Geotherm Res* 80:85–100
- Bedini RM, Bodinier JL (1999) Distribution of incompatible trace elements between the constituents of spinel peridotite xenoliths: ICP-MS data from the East African Rift. *Geochim Cosmochim Acta* 22:3883–3900
- Bedini RM, Bodinier JL, Dautria JM, Morten L (1997) Evolution of LILE-enriched small melt fractions in the lithospheric mantle: a case study from the East African Rift. *Earth Planet Sci Lett* 153:67–83
- Berkthold A, Haak V, Angenheister G (1975) Magnetotelluric measurements in the Afar area. In: Pilger A, Rösler A (eds) *Afar Depression of Ethiopia*. Schweizerbart, Stuttgart, pp 66–79

- Bertrand H, Chazot G, Blichert-Toft J, Thorar S (2003) Implication of widespread high-u volcanism on the Arabian Plate for Afar mantle plume and lithosphere composition. *Chem Geol* 198:47–61
- Betton PJ, Civetta L (1984) Strontium and neodymium isotopic evidence for the heterogeneous nature and development of the mantle beneath Afar (Ethiopia). *Earth Planet Sci Lett* 71:59–70
- Bizzarro M, Baker JA, Haack H, Ulfbeck D, Rosing M (2003) Early history of Earth's crust–mantle system inferred from hafnium isotopes in chondrites. *Nature* 421:931–933
- Blichert-Toft J, Boyet M, Télouk P, Albarède F (2002)  $^{147}\text{Sm}$ – $^{143}\text{Nd}$  and  $^{176}\text{Lu}$ – $^{176}\text{Hf}$  in eucrites and the differentiation of the HED parent body. *Earth Planet Sci Lett* 204:167–181
- Blusztajn J, Hart SR, Shimizu N, McGuire AV (1995) Trace-element and isotopic characteristics of spinel peridotite xenoliths from Saudi Arabia. *Chem Geol* 123:53–65
- Bonatti E, Ottonello G, Hamlyn PR (1986) Peridotites from Zabargad (St. John), Red Sea: petrology and geochemistry. *J Geophys Res* 91:599–631
- Bouvier A, Vervoort JD, Patchett PJ (2008) The Lu–Hf and Sm–Nd isotopic composition of CHUR: constraints from unequilibrated chondrites and implications for the bulk composition of terrestrial planets. *Earth Planet Sci Lett* 273:48–57
- Brey GP, Köhler T (1990) Geothermobarometry in four phase lherzolites. Part II. New thermobarometers and practical assessment of existing thermobarometers. *J Petrol* 31:1353–1378
- Brueckner HK, Zindler A, Seyler M, Bonatti E (1988) Zabargad and the isotopic evolution of the sub-Red Sea mantle and crust. *Tectonophysics* 150:163–176
- Capaldi G, Manetti P, Piccardo GB, Poli G (1987) Nature and geodynamic significance of the Miocene dyke swarms in the North Yemen (YAR). *Neues Jahrb Mineral Abh* 156:207–229
- Chazot G, Bertrand H (1993) Mantle sources and magma–continental crust interactions during early Red Sea–Aden rifting in Southern Yemen: elemental and Sr, Nd, Pb isotope evidence. *J Geophys Res* 98:1819–1835
- Chazot G, Menzies M, Harte B (1996) Silicate glasses in spinel lherzolites from Yemen: origin and chemical composition. *Chem Geol* 134:159–179
- Cimmino F, Pedemonte GM, Piccardo GB (1976) Petrology of ultramafic xenoliths in fissure alkali basalts of the Assab Region (Afar, Ethiopia). *Rend Soc Ital Mineral Petrol* 32:561–577
- Civetta L, De Fino M, La Volpe L, Lirer L (1974) Geochemical trend in the alkali basaltic suite of the Assab range (Ethiopia). *Chem Geol* 13:149–162
- Civetta L, De Fino M, Gasparini P, Ghiara MR, La Volpe L, Lirer L (1975) Structural meaning of east-central Afar volcanism (Ethiopia, T.F.A.I.). *J Geol* 83:363–373
- Condie KC (1999) Mafic crustal xenoliths and the origin of the lower continental crust. *Lithos* 46:95–101
- Conticelli S, Sintoni MF, Abebe T, Mazzarini F, Manetti P (1999) Petrology and geochemistry of ultramafic xenoliths and host basalts from the Ethiopian Volcanic Province: an insight into the upper mantle under Eastern Africa. In: Boccaletti M, Peccerillo A (eds) *The Ethiopian Rift System*, *Acta Volcanol* 11, pp 143–159
- De Fino M, La Volpe L, Lirer L (1973) Volcanology and petrology of the Assab-Range (Ethiopia). *Bull Volcanol* 37:95–110
- Deniel C, Vidal Ph, Coulon C, Vellutini PJ, Pigué P (1994) Temporal evolution of mantle sources during continental rifting: the volcanism of Djibouti (Afar). *J Geophys Res* 99:2853–2869
- Dugda MT, Nyblade AA, Julia J, Langston CA, Ammon CJ, Simiyu S (2005) Crustal structure in Ethiopia and Kenya from receiver function analysis: implications for rift development in eastern Africa. *J Geophys Res* 110:B01303. doi:10.1029/2004JB003065
- Farnetani CG, Richards MA, Ghiorso MS (1996) Petrological models of magma evolution and deep crustal structure beneath hotspots and flood basalt provinces. *Earth Planet Sci Lett* 143:81–94
- Ferrando S, Frezzotti ML, Neumann E-R, De Astis G, Peccerillo A, Dereje A, Gezahegn Y, Teklewold A (2007) Composition and thermal structure of the lithosphere beneath the Ethiopian plateau: evidence from mantle xenoliths in basanites, Injibara, Lake Tana Province. *Mineral Petrol*. doi:10.1007/s00710-007-0219-z
- Griffin WL, Doyle BJ, Ryan CG, Pearson NJ, O'Reilly SY, Davies R, Kivi K, Achterbergh EV, Natapov LM (1999) Layered mantle lithosphere in the Lac de Gras Area, Slave craton: composition, structure and origin. *J Petrol* 40:705–727
- Hart WK, Woldegabriel G, Walter RC, Mertzman SA (1989) Basaltic volcanism in Ethiopia: constraints on continental rifting and mantle interactions. *J Geophys Res* 94:7731–7748
- Henjes-Kunst F, Altherr F, Baumann A (1990) Evolution and composition of the lithospheric mantle underneath the western Arabian peninsula: constraints from Sr–Nd & type systematics of mantle xenoliths. *Contrib Mineral Petrol* 105:460–472
- Hoffman C, Courtillot V, Feraud G, Rochette P, Yirgu G, Ketefo E, Pik R (1997) Timing of the Ethiopian flood basalt event and implications for plume birth and global change. *Nature* 389:838–841
- Ionov DA (1998) Trace element composition of mantle-derived carbonates and coexisting phases in peridotite xenoliths from alkali basalts. *J Petrol* 39:1931–1941
- Ionov DA, Dupuy C, O'Reilly SY, Kopylova MG, Genshaft YS (1993) Carbonated peridotite xenoliths from Spitsbergen: implications for trace element signature of mantle carbonate metasomatism. *Earth Planet Sci Lett* 119:283–297
- Johnson KTM, Dick HJB, Shimizu N (1990) Melting in the oceanic upper mantle: an ion microprobe study of diopsides in abyssal peridotites. *J Geophys Res* 95:2661–2678
- Kurat G, Palme H, Embey-Isztin A, Touret J, Ntaflos T, Spettel B, Brandstätter F, Palme C, Dreibus G, Prinz M (1993) Petrology and geochemistry of peridotites and associated vein rocks of Zabargad island, Red Sea, Egypt. *Mineral Petrol* 48:309–341
- Longerich HP, Jackson SE, Gunther D (1996) Laser ablation inductively coupled plasma mass spectrometric transient signal data acquisition and analyte concentration calculation. *J Anal At Spectrom* 11:899–904
- Mackenzie GH, Thybo GH, Maguire P (2005) Crustal velocity structure across the Main Ethiopian Rift: results from 2-dimensional wide-angle seismic modeling. *Geophys J Int* 162:994–1006
- Makris J, Ginzburg A (1987) The Afar Depression: transition between continental rifting and sea floor spreading. *Tectonophysics* 141:199–214
- Manetti PG, Capaldi G, Chiesa S, Civetta L, Conticelli S, Gasparon M, La Volpe L, Orsi G (1991) Magmatism of the eastern Red Sea margin in the northern part of Yemen from Oligocene to present. *Tectonophysics* 198:181–202
- Manighetti I, Tapponnier P, Gillot PY, Jacques E, Courtillot V, Armijo R, Ruegg J, King G (1998) Propagation of rifting along the Arabia–Somalia plate boundary into Afar. *J Geophys Res* 103:4947–4974
- Manighetti I, Tapponnier P, Courtillot V, Gallet Y, Jacques E, Gillot PY (2001) Strain transfer between disconnected, propagating rifts in Afar. *J Geophys Res* 106:13613–13665
- McDonough WF, Sun S-s (1995) The composition of the Earth. *Chem Geol* 120:223–253
- McGuire AV (1988) The mantle beneath the Red Sea margin: xenoliths from western Saudi Arabia. *Tectonophysics* 150:101–119

- McGuire AV, Coleman RG (1986) The Jabal Tif Layered Gabbro and associated rocks of the Tihama Asir Complex, SW Saudi Arabia. *J Geol* 94:651–665
- Mercier J-CC (1980) Single-pyroxene thermobarometry. *Tectonophysics* 70:1–37
- Orlando A, Abebe T, Manetti P, Santo AP, Corti G (2006) Petrology of mantle xenoliths from Megado and Dilo, Kenya rift, southern Ethiopia. *Ophiolite* 31:71–87
- Ottonello G (1980) Rare earth abundances and distribution in some spinel peridotite xenoliths from Assab (Ethiopia). *Geochim Cosmochim Acta* 44:1885–1902
- Ottonello G, Piccardo GB, Joron JL, Treuil M (1978) Evolution of the upper mantle under the Assab region (Ethiopia), suggestions from petrology and geochemistry of tectonic ultramafic xenoliths and host basaltic lavas. *Geol Rundsch* 67:547–575
- Ottonello G, Piccardo GB, Joron JL, Treuil M (1980) Nature of the deep crust and uppermost mantle under the Assab Region (Ethiopia): inferences from petrology and geochemistry of mafic–ultramafic inclusions. In: *Geodynamic Evolution of the Afro-Arabian Rift System*, Atti dei Convegni Lincei, Accademia Nazionale dei Lincei 47, pp 463–490
- Pearson DG, Canil D, Shirey SB (2004) Mantle samples included in volcanic rocks: xenoliths and diamonds. In: Carlson RW (ed) *Treatise on geochemistry*, vol 2: the mantle and core. Elsevier–Pergamon, Oxford, pp 171–276
- Piccardo GB, Ottonello G (1978) Partial melting effects on coexisting minerals compositions in upper mantle xenoliths from Assab (Ethiopia). *Rend Soc Ital Mineral Petrol* 34:499–526
- Piccardo GB, Messiga B, Vannucci R (1988) The Zabargad peridotite-pyroxenite association: petrological constraints on its evolution. *Tectonophysics* 150:135–162
- Pik R, Deniel C, Coulon C, Yirgu G, Hofmann C, Ayalew D (1998) The northwestern Ethiopian plateau flood basalts: classification and spatial distribution of magma types. *J Volcanol Geotherm Res* 81:91–111
- Pilger A, Rösler A (1975) *Afar Depression of Ethiopia*. Schweizerbart, Stuttgart
- Roger S, Dautria JM, Coulon C, Pik R, Yirgu G, Michard A, Legros P, Ayalew D (1999) An insight on the nature, composition and evolution of the lithospheric mantle beneath in the north-western Ethiopian plateau: the ultrabasic xenoliths from the Tana Lake Province. In: Boccaletti M, Peccerillo A (eds) *The Ethiopian Rift System*. *Acta Volcanol* 11, pp 161–168
- Rollinson HR (1993) *Using geochemical data: evaluation, presentation, interpretation*. Longman, UK
- Rooney TO, Furman T, Yirgu G, Ayalew D (2005) Structure of the Ethiopian lithosphere; xenolith evidence in the main Ethiopian Rift. *Geochim Cosmochim Acta* 69:3889–3910
- Rudnick RL, McDonough WF, Chappell BC (1993) Carbonatite metasomatism in the northern Tanzanian mantle. *Earth Planet Sci Lett* 114:463–475
- Rudnick RL, McDonough WF, O’Connell RJ (1998) Thermal structure, thickness and composition of continental lithosphere. *Chem Geol* 145:395–411
- Schilling JG, Kingsley RH, Hanan BB, McCully BL (1992) Nd–Sr–Pb variations along the Gulf of Aden: evidence for Afar mantle plume–continental lithosphere interaction. *J Geophys Res* 97:10927–10966
- Shaw JE, Baker J, Kent AJR, Ibrahim KM, Menzies MA (2007) The geochemistry of the Arabian lithosphere mantle—a source for intraplate volcanism? *J Petrol* 48:1495–1512
- Teklay M (2006) Neoproterozoic arc–back–arc system analog to modern arc–back–arc systems: evidence from tholeiite–boninite association, serpentinite mudflows and across-arc geochemical trends in Eritrea, southern Arabian–Nubian shield. *Precam Res* 145:81–92
- Teklay M, Kröner A, Mezger K (2001) Geochemistry, geochronology and isotope geology of Nakfa intrusive rocks, northern Eritrea: products of a tectonically thickened Neoproterozoic crust. *J Afr Earth Sci* 33:283–301
- Tiberi C, Ebinger CJ, Ballu V, Stuart G, Oluma B (2005) Inverse models of gravity data from the Red Sea–Aden–East African rifts triple junction zone. *Geophys J Int* 163:775–787
- Ukstins Peate I, Baker JA, Al-Kadasi M, Al-Subbary A, Knight KB, Riisager P, Thirlwall MF, Peate DW, Renne PR, Menzies MA (2005) Volcanic stratigraphy of large-volume silicic pyroclastic eruptions during Oligocene Afro-Arabian flood volcanism in Yemen. *Bull Volcanol* 68:135–156
- Volker F, Altherr R, Jochum KP, McCulloch MT (1997) Quaternary volcanic activity of the southern Red Sea: new data and assessment of models on magma sources and Afar plume–lithosphere interaction. *Tectonophysics* 278:15–29
- Wylie PJ (1981) Plate tectonics and magma genesis. *Geol Rundsch* 70:128–153